The Astrophysical Journal, 743:114 (19pp), 2011 December 20 doi:10.1088/0004-637X/743/2/114

Pan-STARRS1 DISCOVERY OF TWO ULTRALUMINOUS SUPERNOVAE AT $z \approx 0.9$

L. Chomiuk[1,2], R. Chornock[2], A. M. Soderberg[2], E. Berger[2], R. A. Chevalier[3], R. J. Foley[2], M. E. Huber[4], G. Narayan[5], A. Rest[6], S. Gezari[4], R. P. Kirshner[2], A. Riess[4], S. A. Rodney[4], S. J. Smartt[7], C. W. Stubbs[5], J. L. Tonry[8], W. M. Wood-Vasey[9], W. S. Burgett[8], K. C. Chambers[8], I. Czekala[2], H. Flewelling[8], K. Forster[10], N. Kaiser[8], R.-P. Kudritzki[8], E. A. Magnier[8], D. C. Martin[10], J. S. Morgan[8], J. D. Neill[10], P. A. Price[11], K. C. Roth[12], N. E. Sanders[2], and R. J. Wainscoat[8]

[1] National Radio Astronomy Observatory, P.O. Box O, Socorro, NM 87801, USA; lchomiuk@cfa.harvard.edu
[2] Harvard-Smithsonian Center for Astrophysics, 60 Garden Street, Cambridge, MA 02138, USA
[3] Department of Astronomy, University of Virginia, P.O. Box 400325, Charlottesville, VA 22904-4325, USA
[4] Department of Physics and Astronomy, Johns Hopkins University, 3400 North Charles Street, Baltimore, MD 21218, USA
[5] Department of Physics, Harvard University, Cambridge, MA 02138, USA
[6] Space Telescope Science Institute, 3700 San Martin Drive, Baltimore, MD 21218, USA
[7] Astrophysics Research Centre, School of Mathematics and Physics, Queen's University Belfast, Belfast BT7 1NN, UK
[8] Institute for Astronomy, University of Hawaii at Manoa, Honolulu, HI 96822, USA
[9] Department of Physics and Astronomy, University of Pittsburgh, 3941 O'Hara Street, Pittsburgh, PA 15260, USA
[10] California Institute of Technology, 1200 E. California Blvd., Pasadena, CA 91125, USA
[11] Department of Astrophysical Sciences, Princeton University, Princeton, NJ 08544, USA
[12] Gemini Observatory, 670 North A'ohoku Place, Hilo, HI 96720, USA
Received 2011 July 3; accepted 2011 September 14; published 2011 November 29

ABSTRACT

We present the discovery of two ultraluminous supernovae (SNe) at $z \approx 0.9$ with the Pan-STARRS1 Medium Deep Survey. These SNe, PS1-10ky and PS1-10awh, are among the most luminous SNe ever discovered, comparable to the unusual transients SN 2005ap and SCP 06F6. Like SN 2005ap and SCP 06F6, they show characteristic high luminosities ($M_{\rm bol} \approx -22.5$ mag), blue spectra with a few broad absorption lines, and no evidence for H or He. We have constructed a full multi-color light curve sensitive to the peak of the spectral energy distribution in the rest-frame ultraviolet, and we have obtained time series spectroscopy for these SNe. Given the similarities between the SNe, we combine their light curves to estimate a total radiated energy over the course of explosion of (0.9–1.4) $\times 10^{51}$ erg. We find photospheric velocities of 12,000–19,000 km s^{-1} with no evidence for deceleration measured across $\sim$3 rest-frame weeks around light curve peak, consistent with the expansion of an optically thick massive shell of material. We show that, consistent with findings for other ultraluminous SNe in this class, radioactive decay is not sufficient to power PS1-10ky, and we discuss two plausible origins for these events: the initial spin-down of a newborn magnetar in a core-collapse SN, or SN shock breakout from the dense circumstellar wind surrounding a Wolf–Rayet star.

Key words: circumstellar matter – stars: magnetars – supernovae: general – supernovae: individual (PS1-10ky, PS1-10awh)

Online-only material: color figures

1. INTRODUCTION

The observational and physical parameter space occupied by supernovae (SNe) has expanded dramatically because of the recent discovery of several ultraluminous SNe. These SNe are significantly more luminous than SN explosions of Type Ia, displaying absolute bolometric magnitudes at light curve maximum of < -21 mag and total radiated energies on the order of 10^{51} erg. Thus far, ultraluminous SNe have displayed impressive diversity, ranging from the Type Ic SN 2007bi, proposed to be a pair-instability explosion (Gal-Yam et al. 2009; Young et al. 2010), to the Type IIn SN 2006gy, with strong signs of circumstellar interaction (Ofek et al. 2007; Smith et al. 2007; Smith & McCray 2007).

One of the earliest ultraluminous SN discoveries, SN 2005ap (Quimby et al. 2007), showed a peak luminosity of $\sim 4 \times 10^{44}$ erg s^{-1}, limited evidence for H or He, and a blue continuum with a distinctive "W"-shaped spectral feature at $\sim$4200 Å. Subsequently, the mysterious transient SCP 06F6 was discovered by Barbary et al. (2009), showing a largely featureless spectrum with a few broad absorption lines, and proving so perplexing that initially the redshift was unclear. Because it was uncertain if the source was Galactic or at a cosmological distance, many ideas were presented to explain it ranging from an outburst on a white dwarf to a broad-lined QSO (Barbary et al. 2009; Gänsicke et al. 2009; Chatzopoulos et al. 2009; Soker et al. 2010).

Recently, SN 2005ap and SCP 06F6 were tied together into a common class of transients by Quimby et al. (2011, henceforth Q+11), who collected four additional SN 2005ap-like sources discovered by the Palomar Transient Factory (PTF). They identified narrow Mg II λλ2796,2803 absorption lines in their spectra, presumably associated with the interstellar media of the host galaxies. From this absorption, they derived redshifts ranging from $0.23 < z < 1.19$ for the sample. These cosmological distances imply that the SN 2005ap-like sources are some of the most luminous SNe known, with peak absolute magnitudes $M_U \lesssim -22$ mag and total radiated energies $\gtrsim 10^{51}$ erg.

With their redshifts known, a common set of observational properties began to emerge for the SN 2005ap-like objects. In addition to their very high peak luminosities, these sources typically show distinctive symmetric light curves with rise times of $\sim$20–50 of days in the rest frame. They also all show blue

spectra with only a handful of features; Q+11 identify the broad absorption lines with light metals (C, O, Si, and Mg). There is no clear evidence for H or He in the spectra of an SN 2005ap-like transient (Quimby et al. 2007 noted a broad feature in SN 2005ap and initially associated it with Hα, but more recently Q+11 identified it with C II). There also is no detection of strong Fe II or Fe III lines in the early or peak spectra of these transients.

One of these sources, SN 2010gx/PTF10cwr, displays SN 2005ap-like spectral features and high luminosity at early times (Pastorello et al. 2010; Q+11). At later times (a few weeks after peak light), Pastorello et al. find that this source shows iron and other features characteristic of ordinary Type Ic SNe. They assert that SN 2005ap-like objects are likely to be associated with SNe Ibc, consistent with the lack of H in their spectra. Additional evidence for an association with SNe Ibc comes from PTF09cnd; Q+11 observed its late-time (Day 115) spectrum and find that it is consistent with the spectrum of a very slowly evolving SN Ic.

Two potential explanations for these SN 2005ap-like sources have surfaced: the interaction of the SN shock with a dense circumstellar shell of H-poor material (e.g., Chevalier & Irwin 2011) or the spin-down of a newborn magnetar embedded in the SN ejecta (Kasen & Bildsten 2010; Woosley 2010). Both of these models have the potential to explain the high luminosities and association with SNe Ibc.

Here, we present the discovery and detailed follow-up of two new ultraluminous SNe at $z \approx 0.9$ revealed in 2010 by the Panoramic Survey Telescope & Rapid Response System 1 (Pan-STARRS1, abbreviated as PS1 here). By combining data for these two sources, we obtain thorough multi-band light curve coverage for a composite SN 2005ap-like object and measure its color evolution. Meanwhile, the sources' high redshifts allow us to obtain the highest-quality measurements to date of the bolometric luminosity of an SN 2005ap-like explosion, as these sources' spectral energy distributions (SEDs) peak in the rest-frame ultraviolet. Our spectroscopic observations sample the light curve across its peak (from Day -21 to Day 26), enabling us to measure the evolution of photospheric velocities. These measurements place important constraints on any model that attempts to explain these sources' high luminosities.

In Section 2, we describe our data, obtained using PS1, the MMT and Gemini Observatories, *Galaxy Evolution Explorer* (*GALEX*), and the Expanded Very Large Array (EVLA). In Section 3, we constrain the properties of the host galaxies. In Sections 4–6, we measure the evolution of their effective color temperatures, bolometric luminosities, and photospheric velocities. In Section 7, we consider three possible physical scenarios that might explain the characteristics of these sources: radioactive decay, magnetar spin-down, and circumstellar interaction. Finally in Section 8, we summarize our results.

2. OBSERVATIONS

2.1. PS1 Photometry

2.1.1. PS1 Survey Summary

The PS1 system is a high-etendue wide-field imaging system, designed for dedicated survey observations. The system is installed on the peak of Haleakala on the island of Maui in the Hawaiian island chain. Routine observations are conducted remotely, from the Waiakoa Laboratory in Pukalani. A complete description of the PS1 system, both hardware and software, is provided by Kaiser et al. (2010). The survey design and execution strategy are described in K. C. Chambers et al. (2011, in preparation).

The PS1 optical design (Hodapp et al. 2004) uses a 1.8 m diameter f4.4 primary mirror, and a 0.9 m secondary. The resulting converging beam then passes through two refractive correctors, a 48 cm $\times$ 48 cm interference filter, and a final refractive corrector that is the dewar window. The telescope delivers an image with a diameter of 3.°3, with low distortion. The PS1 imager (Tonry & Onaka 2009) comprises a total of 60 4800 $\times$ 4800 pixel detectors, with 10 μm pixels that subtend 0.258 arcsec, providing an instantaneous field of view of 7.1 deg^2. The detectors are back-illuminated CCDs manufactured by Lincoln Laboratory. The detectors are read out using a StarGrasp CCD controller, with a readout time of 7 s for a full unbinned image. Initial performance assessments are presented in Onaka et al. (2008).

The PS1 observations are obtained through a set of five broadband filters, which we have designated as $g_{\rm P1}$, $r_{\rm P1}$, $i_{\rm P1}$, $z_{\rm P1}$, and $y_{\rm P1}$. Although the filter system for PS1 has much in common with that used in previous surveys, such as Sloan Digital Sky Survey (SDSS; York et al. 2000; Abazajian et al. 2009), there are important differences. The $g_{\rm P1}$ filter extends 200 Å redward of $g_{\rm SDSS}$, paying the price of 5577 Å sky emission for greater sensitivity and lower systematics for photometric redshifts, and the $z_{\rm P1}$ filter is cut off at 9200 Å, giving it a different response than the detector response defined $z_{\rm SDSS}$. SDSS has no corresponding $y_{\rm P1}$ filter. Further information on the passband shapes is described in Stubbs et al. (2010). Provisional response functions (including 1.3 airmasses of atmosphere) are available at the project's web site.[13] Photometry is in the "natural" PS1 system, $m = -2.5\ \log(\text{flux}) + m'$, with a single zero-point adjustment m' made in each band to conform to the AB magnitude scale. Zero points were measured from comparison with field stars in the SDSS catalog, but no color corrections were made to determine the magnitudes exactly in the SDSS system.

The PS1 Medium Deep Survey (MDS) accounts for approximately 25% of observing time. It revisits 10 fields (each equivalent to a single PS1 imager footprint) on a nearly nightly basis in $g_{\rm P1}$, $r_{\rm P1}$, $i_{\rm P1}$, $z_{\rm P1}$, and $y_{\rm P1}$ bands (Stubbs et al. 2010), reaching a typical 5σ limiting magnitude of $\sim$23.3 mag in one visit at $g_{\rm P1}$, $r_{\rm P1}$, $i_{\rm P1}$, and $z_{\rm P1}$ bands and $\sim$21.7 mag in $y_{\rm P1}$. The MDS fields are distributed across the sky, so only a subset of fields are observed at any given time of year, and on any given night only in a subset of bands, depending on observing conditions.

The MDS images are processed through the Image Processing Pipeline (IPP; Magnier 2006), on a computer cluster at the Maui High Performance Computer Center. The pipeline runs the images through a succession of stages, including flat fielding ("de-trending"), a flux-conserving warping to a sky-based image plane, masking and artifact removal, and object detection and photometry. Difference images are produced from the stacked images by the `photpipe` pipeline (Rest et al. 2005) and potential transients are visually inspected by humans for possible promotion to the status of transient alerts. The IPP-photpipe system finds hundreds of transient alerts per month, of which a subset is targeted for spectroscopic confirmation.

2.1.2. PS1-10ky and PS1-10awh

PS1-10awh and PS1-10ky were discovered by the PS1 MDS at J2000 locations of R.A. = $22^{\rm h}14^{\rm m}29\overset{\rm s}{.}831$, decl. = $-00°04'03\overset{''}{.}62$ and R.A. = $22^{\rm h}13^{\rm m}37\overset{\rm s}{.}851$, decl. = $+01°14'23\overset{''}{.}57$,

[13] http://svn.pan-starrs.ifa.hawaii.edu/trac/ipp/wiki/PS1_Photometric_System

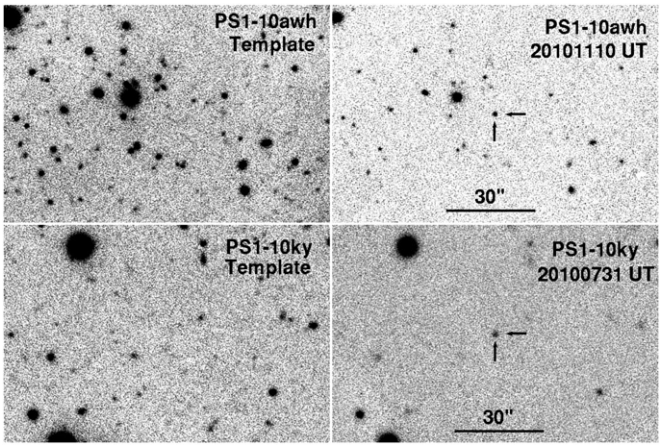

Figure 1. Cutouts of PS1 i_{P1}-band images showing the region around PS1-10awh (top) and PS1-10ky (bottom). The left column shows stacked images using data before explosion; the right column shows images from single nights around maximum light.

respectively (uncertainty in positions $\approx$ 0.05 arcsec). PS1-10ky was apparent immediately when observations began of the MD09 field in 2010 June. It was discovered near peak brightness and had faded below PS1 MDS sensitivity by 2010 November. PS1-10awh was first detected in early 2010 October by its rising flux, and was observed almost every night by PS1 MDS until Field MD09 set in early December. Figure 1 shows the vicinities of the SNe before explosion and around maximum light. Both objects were selected for spectroscopic follow-up at the MMT and Gemini based on the lack of visible host galaxies in the template images and were then confirmed as high-redshift SNe.

`Photpipe` measures SN photometry using forced-centroid point-spread function (PSF) fitting photometry on the difference images, with a PSF appropriate to each difference image, and a common centroid derived from the high signal-to-noise ratio (S/N) detections. The measured AB magnitudes for PS1-10awh and PS1-10ky are listed in Table 4 below and plotted in Figure 2, along with 5σ upper limits for epochs with non-detections. We corrected for foreground extinction using Schlegel et al. (1998) values and the Cardelli et al. (1989) extinction law, but did not correct for any intrinsic extinction.

To calculate absolute magnitudes, we did not carry out a full k-correction, but instead only corrected the measured magnitudes for cosmological expansion using the redshifts measured from Mg II absorption (Section 2.2). The spectral luminosity in the emitted frame ($L_\nu(\nu_e)$; units of erg s^{-1} Hz^{-1}) can be expressed as $L_\nu(\nu_e) = \frac{4\pi\ d_L^2}{1+z} f_\nu(\nu_o)$, where z is the redshift, d_L is the luminosity distance, and $f_\nu(\nu_o)$ is the observed flux density in the observer's frame in cgs units. This yields an expression for the absolute AB magnitude (Hogg et al. 2002): $M = m - 5\ \log\left(\frac{d_L}{10\ \mathrm{pc}}\right) + 2.5\ \log(1+z)$, where m is the apparent AB magnitude. We did not shift the central wavelengths at which flux densities were measured (see Table 1 for central wavelengths in the rest frame, which are weighted by the system response). The similar redshifts of PS1-10ky ($z = 0.956$) and PS1-10awh ($z = 0.908$) ensure that the rest wavelengths and passbands of the photometry are comparable.

The light curves show similar peak luminosities, widths, and color evolution. We find that we can splice them together to produce a full light curve if we set the peak date to 2010 July 20 for PS1-10ky and to 2010 November 15 for PS1-10awh (Figure 3). For both objects, we observe the peak of the light curve in at least both the g_{P1} and z_{P1} bands, implying that PS1-10awh represents the light curve rise and PS1-10ky samples the light curve decline (we assume a single and smooth light curve peak, motivated by other light curves published for SN 2005ap-like objects; Barbary et al. 2009; Q+11). We have overlapping light curve coverage for $\sim$21 rest-frame days around peak (see hatched region in Figure 3). The splicing of the light curves is well constrained by a few late-time measurements of PS1-10awh: notably the z_{P1} measurement from 2010 December 10 and the g_{P1} upper limit from 2010 December 5, which both show a declining light curve (Figure 2). Note the rapid falloff in the g_{P1} band for both sources (Figure 3), implying that they have a similar color evolution (although PS1-10awh does appear to fall off a bit faster than PS1-10ky). Uncertainties in the splicing (or in our implicit assumption that these two sources are very similar) will affect comparisons of the rise and the decline (as needed for a full fit to the magnetar model; Section 7.2), and also introduce uncertainty into the integrated radiated energy calculated in Section 5.

Table 1
Central Rest Wavelengths of Optical Passbands (Å)

Filter[a]	PS1-10awh	PS1-10ky	SN 2010gx	SCP 06F6
u	...	...	2878	...
g	2550	2488	3878	...
r	3267	3188	5065	...
i	3944	3848	6199	3540
z	4536	4426	7426	3883
y	5097	4974	...	...

Note.
[a] These are PS1 filters (Stubbs et al. 2010) for PS1-10ky and PS1-10awh, SDSS filters for SN 2010gx, and *Hubble Space Telescope* Advanced Camera for Surveys filters F775W and F850LP for SCP 06F6.

In Figure 4, we compare the combined light curve from PS1-10ky and PS1-10awh with one of the first ultraluminous transients discovered, SCP 06F6 (Barbary et al. 2009; Q+11; $z = 1.19$), and two sources with exceptionally high-quality observations: SN 2010gx (Pastorello et al. 2010; Q+11; $z = 0.23$) and PTF09cnd (Q+11; $z = 0.26$). For SCP 06F6 and SN 2010gx, we show single-band measurements converted to absolute magnitudes as described above (Equation (2)), as the redshifts and photometric coverage of these events lead to measurements with similar central rest-frame wavelengths as our i_{P1} (and g_{P1}, in the case of SN 2010gx) measurements of PS1-10ky and PS1-10awh. For PTF09cnd, we plot the rest-frame u-band light curve calculated by Q+11.

The top panel of Figure 4 shows light curves at redder wavelengths ($\sim$3900 Å rest frame), and we see that there is significant dispersion in the light curve widths of SN 2005ap-like objects (this was also pointed out by Q+11). PTF09cnd shows one of the broadest light curves yet observed for an SN 2005ap-like object, with a rise time of $\sim$55 days, while a few early R-band observations of SN 2010gx by Q+11 show that this source rises quite rapidly (rise time $\approx$ 20 days). The PS1 objects presented here display light curves of slightly broader width; the rise time for PS1-10awh is $\sim$25 days. The combination of our two PS1 SNe show a light curve that falls off much more slowly at the redder ($\sim$3900 Å; top panel) bands, as compared with the bluer ($\sim$2500 Å; bottom panel) measurements. The light curve of SN 2010gx also shows the bluer filter declining much faster than the redder, in good accord with PS1-10ky and PS1-10awh. The single-band peak luminosities of the five sources agree to within $\sim$30%.

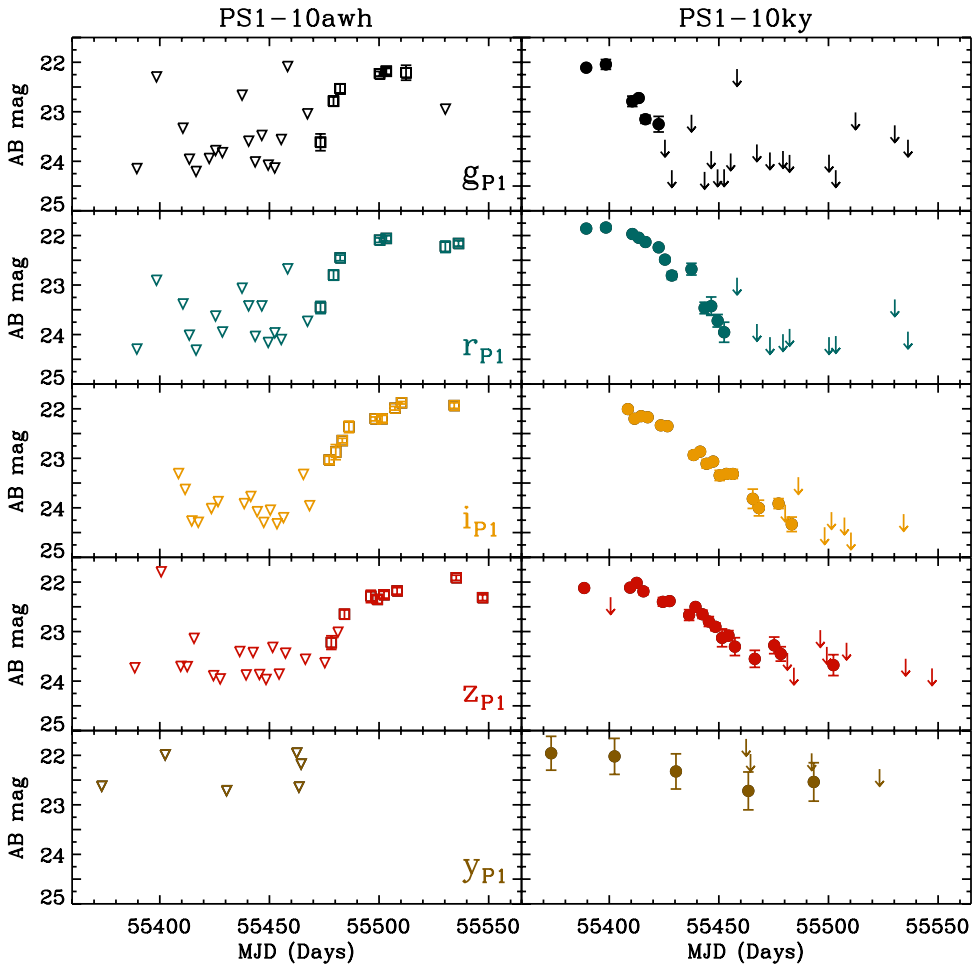

Figure 2. Observed light curves for PS1-10awh (left column) and PS1-10ky (right column) in five filters from top to bottom: g_{P1} (black), r_{P1} (blue), i_{P1} (gold), z_{P1} (red), and y_{P1} (brown). Apparent AB magnitudes are plotted as a function of modified Julian day, with squares and circles representing PS1-10awh and PS1-10ky, respectively, and 5σ upper limits denoted by triangles and arrows.

(A color version of this figure is available in the online journal.)

Table 2
Spectroscopic Observations

Date	Phase[a] (Days)	Facility	Grating/ Central λ (Å)	λ Range[b] (Å)	Res[c] (Å)	Airmass	Slit P.A. (deg)
PS1-10ky							
2010 Jul 17	−2	MMT/Blue Channel[d]	300/6006	3393–8623	5.5	1.2	326
2010 Jul 21	1	Gemini-N/GMOS[e]	B600/4800	3390–6220	4.7	1.1	180
2010 Aug 18	15	Gemini-S/GMOS	B600/5000	3600–6432	4.7	1.3	180
2010 Sep 9	26	Gemini-S/GMOS	R400/8000	5887–10161	8.0	1.4	180
PS1-10awh							
2010 Oct 12	−21	Gemini-N/GMOS	R400/7500	5441–9655	5.0	1.3	210
2010 Nov 27	4	MMT/Hectospec[f]	270/6500	3700–9150	4.9	1.2	Fiber
2010 Dec 9	10	MMT/Blue Channel	300/5768	3230–8325	5.5	1.5	40

Notes.
[a] In the rest frame.
[b] In the observer frame.
[c] Approximate spectral resolution, measured from widths of night-sky lines.
[d] Schmidt et al. (1989).
[e] Hook et al. (2004).
[f] Fabricant et al. (2005).

2.2. *Spectroscopy*

We obtained four optical spectra of PS1-10ky and three spectra of PS1-10awh using MMT (Hectospec and Blue Channel Spectrographs; Fabricant et al. 2005; Schmidt et al. 1989) and Gemini (GMOS; Table 2). Basic spectroscopic processing and extraction were accomplished using standard routines in IRAF, or using the OIR Telescope Data Center pipeline in the case

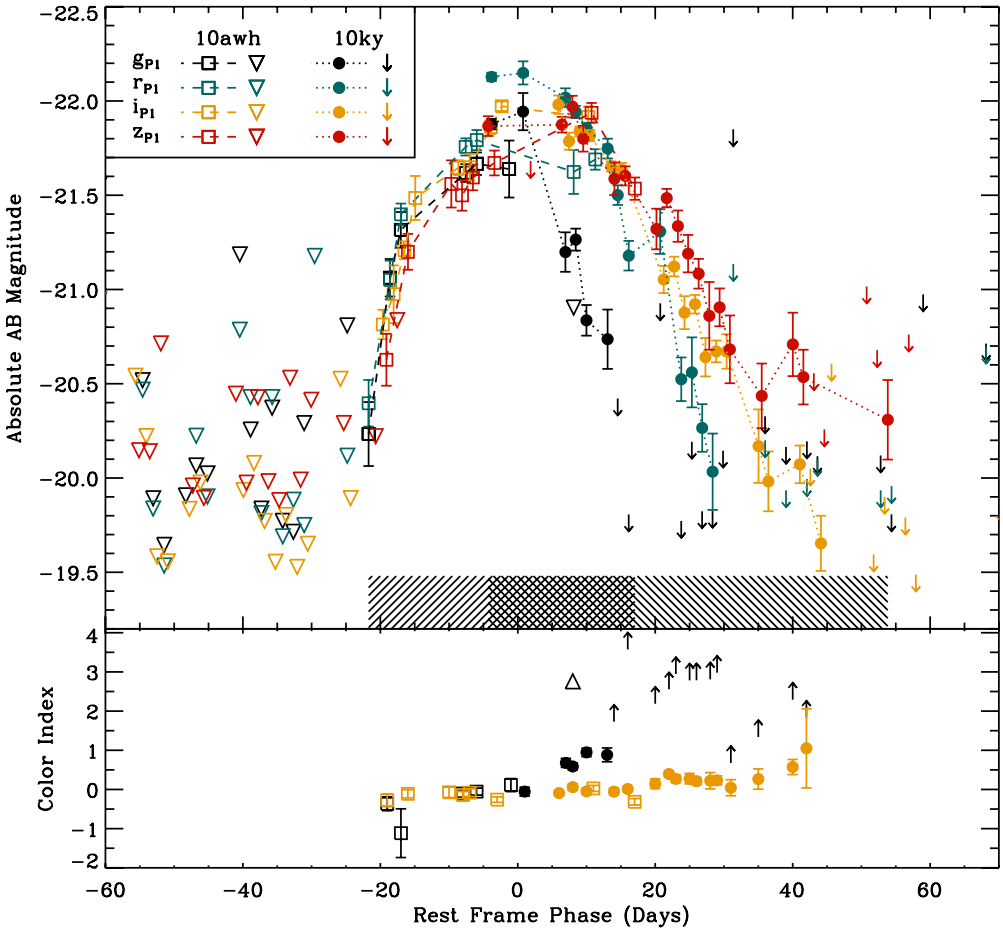

Figure 3. Top panel: combined light curve for PS1-10awh and PS1-10ky in four filters that have been redshifted to the central wavelengths listed in Table 1: g_{P1} (black), r_{P1} (blue), i_{P1} (gold), and z_{P1} (red). Measurements for PS1-10awh are marked as open squares connected with dashed lines; 5σ upper limits are denoted by open triangles. For PS1-10ky, measurements are shown as filled circles connected with dotted lines, and upper limits are signified with arrows. Rest-frame times and absolute magnitudes are calculated using measured redshifts of $z = 0.908$ and $z = 0.956$, respectively. To highlight the overlap of the two light curves, the time ranges during which each SN is detected in PS1 photometry are marked as hatched regions at the bottom of the plot. Bottom panel: the time evolution of $g_{P1} - z_{P1}$ color in black and $i_{P1} - z_{P1}$ color in gold. Measurements and limits for PS1-10awh are marked as squares and triangle, respectively, while measurements and limits for PS1-10ky are shown as circles and arrows.

of MMT/Hectospec data (Mink et al. 2007). We then used custom IDL routines to apply flux calibrations and remove telluric absorption based on observations of spectrophotometric standard stars. Narrow Mg II λλ2796,2803 absorption, arising from the interstellar medium of the SN host galaxy, is seen in all spectra with wavelength coverage of the doublet (Figure 5). From this absorption, we measure a redshift of $z = 0.9084$ for PS1-10awh and $z = 0.9558$ for PS1-10ky. These correspond to luminosity distances of $d_L = 5890$ Mpc and $d_L = 6270$ Mpc for a cosmology with $H_0 = 71$ km s^{-1} Mpc^{-1}, $\Omega_M = 0.27$, and $\Omega_\Lambda = 0.73$.

The spectra are shown in Figure 6, along with the SCP 06F6 spectra from Barbary et al. (2009), spectra of SN 2010gx from Pastorello et al. (2010), and spectra of PTF09cnd from Q+11. As with the photometry, we corrected them for foreground extinction (Schlegel et al. 1998; Cardelli et al. 1989). In many cases, clouds were present during observations so the absolute flux scaling of the spectra cannot be trusted, but the general shape of the continuum is reliable.

The three broad absorption features between 2000 and 2900 Å were identified by Q+11 as C II (∼2330 Å), Si III (2543 Å), and Mg II (2800 Å). The broad "W"-shaped feature around 4300 Å was first seen in SN 2005ap (Quimby et al. 2007) and at very early times in SN 2008D (Malesani et al. 2009; Modjaz et al. 2009), and was tentatively associated with a combination of C III, N III, and O III by these authors. More recently, Q+11 found that this feature was widely displayed across their sample of SN 2005ap-like objects, and identified it with a single ion, O II. This "W" feature can be seen in the GMOS spectrum of PS1-10awh observed on Day −21.

Note that PS1-10ky and PS1-10awh show spectral features that become weaker as time progresses; our later spectra on PS1-10ky appear almost featureless. In SN 2010gx, the 4300 Å "W" feature has disappeared and the spectrum is practically featureless by Day 4, but then subsequently it shows strong SN Ic-like features of Fe II, Ca II, and Mg II. PTF09cnd also shows an SN Ic-like spectrum at late time (Day 115), but, as pointed out by Q+11, the spectrum seems to have evolved very slowly as compared with typical SNe Ic. The similarities between the SN 2010gx spectrum at Day 30 and the PTF09cnd spectrum at Day 115 are striking (Figure 6), and imply that there is significant dispersion between SN 2005ap-like objects as to how quickly their spectra evolve, likely associated with the dispersion in the widths of their light curves.

We are not very sensitive to similar SN Ic-like features in PS1-10ky and PS1-10awh because of our blue rest-frame wavelength coverage (Figure 6). Our last spectrum, observed with relatively red wavelength coverage, was observed 26 days after peak and

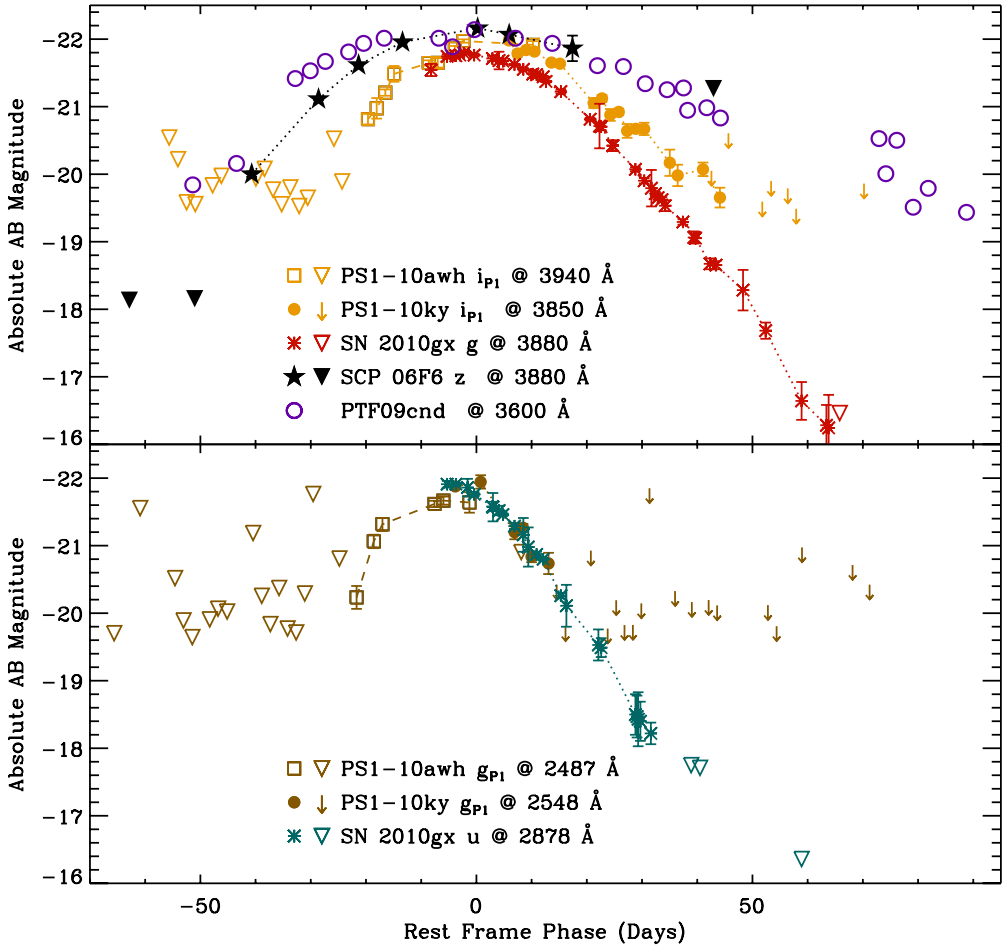

Figure 4. Top panel: a comparison of light curves for SN 2005ap-like ultraluminous SNe. In the top panel, we compare i_{P1}-band light curves for PS1-10awh and PS1-10ky with SN 2010gx g-band measurements and SCP 06F6 z-band measurements, all of which fall at comparable rest wavelengths around 3900 Å. We also overplot the rest-frame u-band light curve for PTF09cnd from Q+11, which probes a similar wavelength of ∼3600 Å. Bottom panel: we compare the g_{P1}-band measurements of PS1-10awh and PS1-10ky with the u-band light curve of SN 2010gx, to probe blue wavelengths around ∼2600 Å (no bluer photometry is available for SCP 06F6 or PTF09cnd).

(A color version of this figure is available in the online journal.)

is rather noisy, but may show low S/N depressions around rest wavelengths of 4350 Å and 4900 Å, potentially consistent with the Fe II and Mg II features in SN 2010gx.

It is remarkable that no lines of H or He have ever been detected from an SN 2005ap-like object, although we note that none of our spectra of PS1-10ky and PS1-10awh cover Hα, and the few that provide coverage of Hβ are very noisy. Similarly with He, the strongest lines are redward of 5000 Å and outside our spectroscopic coverage. However, the spectra obtained on low-redshift SN 2005ap-like objects by Q+11 and Pastorello et al. (2010) do cover this red portion of the spectrum, and no trace of H or He has been detected in these studies.

2.3. GALEX Photometry

MD09 was observed with *GALEX* in 2010 August–September. Both PS1-10ky and PS1-10awh—and their hosts—were non-detections in the NUV band. PS1-10ky was observed by *GALEX* near optical peak brightness, but PS1-10awh was observed before its rise. NUV 5σ upper limits are listed in Table 4. The upper limits of $\gtrsim$ 23.0 mag (AB system) correspond to a luminosity limit of $\lesssim 1.7 \times 10^{41}$ erg s^{-1} Å^{-1} at a central rest wavelength of 1161 Å for PS1-10ky.

2.4. EVLA Radio Continuum Measurements

We observed both ultraluminous SNe with the EVLA (Perley et al. 2011) as part of our NRAO Key Science Project "Exotic Explosions, Eruptions, and Disruptions: A New Transient Phase-Space." We observed at 4.9 GHz with 256 MHz of bandwidth; time on source was 37 minutes for both sources. Gains were calibrated using J2212+0152, and the absolute flux density scale was calibrated using 3C48. PS1-10awh was observed on 2010 December 12, approximately three weeks after optical peak (observer frame), and yielded a non-detection of -22 ± 15 μJy beam^{-1}. PS1-10ky was observed on 2011 February 12, almost seven months after peak; we measured a non-detection of -2 ± 17 μJy beam^{-1} at its location.

The gamma-ray burst (GRB) 030329 would have had a peak 4.9 GHz flux density of ∼200 μJy at the distance of our ultraluminous SNe, and would have remained a $>3\sigma$ source for ∼100 days (Berger et al. 2003; Frail et al. 2005; van der Horst et al. 2005). On the other hand, a weak GRB like 980425 and its associated SN 1998bw would be significantly below our detection limit, with a 4.8 GHz peak flux density of 2 μJy at a distance of 6000 Mpc (Kulkarni et al. 1998). It is unlikely, although not impossible given the spread in GRB

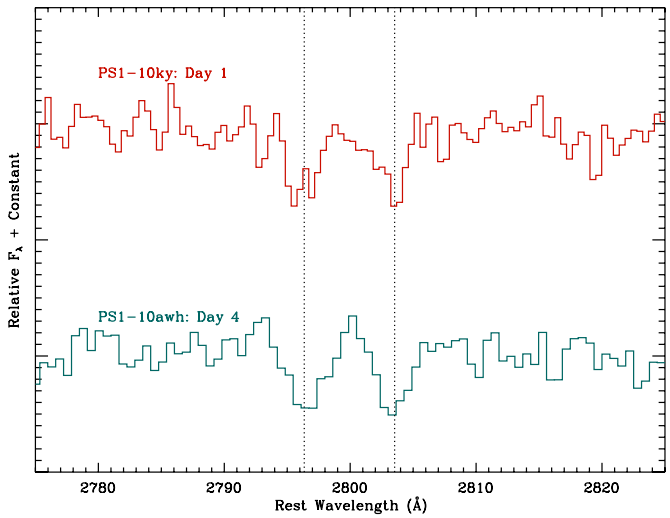

Figure 5. Detail of two spectra with wavelength coverage of the Mg II λλ2796,2803 doublet, redshifted to $z = 0.9084$ for PS1-10awh and $z = 0.9558$ for PS1-10ky. The rest wavelengths of the Mg II doublet are shown as vertical dotted lines.

(A color version of this figure is available in the online journal.)

radio luminosities (Frail et al. 2003), that either PS1-10awh or PS1-10ky hosted a GRB.

3. HOST GALAXIES

We stacked the pre-explosion images of PS1-10awh (prior to 2010 September 21) to derive upper limits on the host galaxy's luminosity. We find 5σ upper limits on apparent magnitude of $g_{\rm P1} > 25.3$, $r_{\rm P1} > 25.3$, $i_{\rm P1} > 25.4$, $z_{\rm P1} > 24.8$, and $y_{\rm P1} > 22.8$ mag. Our $z_{\rm P1}$-band limit roughly corresponds to $M_B > -18.4$ mag or $< 0.07\ L^\star$ (assuming $M_B^\star = -21.3$ mag at a redshift of 0.9; Faber et al. 2007). Similarly, we stacked the 2009 data for PS1-10ky and found apparent magnitude limits of $g_{\rm P1} > 24.8$, $r_{\rm P1} > 24.7$, $i_{\rm P1} > 24.6$, $z_{\rm P1} > 24.0$, and $y_{\rm P1} > 22.1$ mag. The $z_{\rm P1}$-band limit translates to $M_B > -19.4$ mag or $< 0.17\ L^\star$.

The $g_{\rm P1}$ band is centered at ∼2500 Å, in the NUV spectral range commonly used as a tracer of the photospheres of young massive stars, and thereby star formation rate (SFR). Using the calibration of Kennicutt (1998) and assuming no dust extinction, our limits on the $g_{\rm P1}$-band host galaxy luminosities translate to SFR $< 1.3\ M_\odot\ {\rm yr}^{-1}$ for PS1-10ky and $< 1.0\ M_\odot\ {\rm yr}^{-1}$ for PS1-10awh. We also stacked the three spectra for PS1-10awh and detected [O II]λ3727 emission at a luminosity of $(4.5 \pm 1.0) \times 10^{40}$ erg s^{-1}. This translates to an SFR of $0.4 \pm 0.2\ M_\odot\ {\rm yr}^{-1}$ (Kewley et al. 2004), consistent with the NUV limits. We did not stack the PS1-10ky spectra, as the redshift of this source places the [O II] emission line on a telluric feature.

These constraints are consistent with the host galaxies of other ultraluminous SNe (Neill et al. 2011; Stoll et al. 2011), which typically have low masses (less than the Large Magellanic Cloud), relatively low SFRs (70% of the Neill et al. sample has SFR $<1\ M_\odot\ {\rm yr}^{-1}$), and high specific SFRs. This preference for low-mass hosts is reminiscent of GRBs, which also display a bias toward lower-mass hosts with high specific SFR (e.g., Le Floc'h et al. 2003; Fruchter et al. 2006; Christensen et al. 2004). In the context of GRBs, this bias is often attributed to a collapsar origin (MacFadyen & Woosley 1999). The mass–metallicity relationship for galaxies (Tremonti et al. 2004) implies that lower-mass galaxies will be more metal-poor, and metal-poor SN progenitors will undergo less wind-driven mass loss and maintain more angular momentum. However, another recent hypothesis has been offered in which lower metallicity galaxies tend to display higher specific SFRs, implying that the observed bias of GRBs (and perhaps ultraluminous SNe) toward low-metallicity hosts may be explained, at least in part, by a simple association with young stellar populations (Kocevski & West 2011; Mannucci et al. 2011).

4. COLOR EVOLUTION

In order to understand the basic physical parameters of these ultraluminous SNe, we need to constrain their temperature evolution. The SEDs of SN 2005ap-like objects can be reasonably fit as blackbodies at redder wavelengths, but appear to suffer line blanketing blueward of 3000 Å. This was pointed out for SN 2010gx by Pastorello et al. (2010) and is apparent in Figure 7, where we show a spectrum of PS1-10ky with a blackbody fit to the full spectrum ($T = 10{,}400$ K) and a fit to the spectrum redward of 3000 Å ($T = 13{,}400$ K). Clearly, no good blackbody fit is achievable when the bluest wavelengths are included, and the luminosity at $\lesssim 2500$ Å is significantly damped from what is expected for the blackbody fit to the redder wavelengths. All of the spectra in Figure 6 turn over blueward of 3000 Å, so we fit blackbodies to our data redward of 3000 Å.

We carried out least-squares fits of Planck functions to the spectra shown in Figure 6; the best-fit temperatures and errors are listed in Table 3. We also fit color temperatures to the photometric data points for PS1-10awh and PS1-10ky by interpolating the measured fluxes in time with a cubic spline and then least-squares fitting a blackbody spectrum on each rest-frame day which is constrained by measurements at three or more bands with central wavelengths redward of 3000 Å. An interpolated flux on a given day is considered "constrained" if there is a $>5\sigma$ measurement both preceding it and following it in time. Temperature fits are shown in the top panel of Figure 8.

The spectroscopic and photometric temperature measurements agree rather well for PS1-10ky and PS1-10awh, and the color temperatures of all five ultraluminous SNe are roughly consistent with one another. The temperature evolution is modeled with a quadratic fit to the combined measurements for PS1-10ky and PS1-10awh (solid black line in Figure 8) showing a maximum temperature of ∼21,000 K at early times (with significant uncertainty) and a minimum temperature of ∼5000 K at late times.

From Figure 7, we see that even in the absence of line blanketing, we would not expect *GALEX* detections with <23.0 mag (corresponding to $\gtrsim 1.7 \times 10^{41}$ erg s^{-1} Å^{-1} at 1161 Å). The first *GALEX* observation of PS1-10ky occurred at ∼6 days after maximum, when the temperature was cooler and the ultraviolet luminosity would have been even fainter than that predicted in Figure 7.

We note that the C II and Si III absorption have largely disappeared by Day 10, whereas the Mg II absorption is still strong (Figure 6). This might be explained by a cooling photosphere, as Mg II has a lower ionization potential (7.6 eV) than C II (11.3 eV) or Si III (16.4 eV). Similarly, the O II lines have become weaker by Day 4, consistent with its rather high-ionization potential of 13.6 eV. Also, the source of the line blanketing blueward of 3000 Å remains an interesting mystery, as line blanketing is usually caused by Fe-peak elements, but there are no iron lines apparent in the spectra during or preceding light curve maximum.

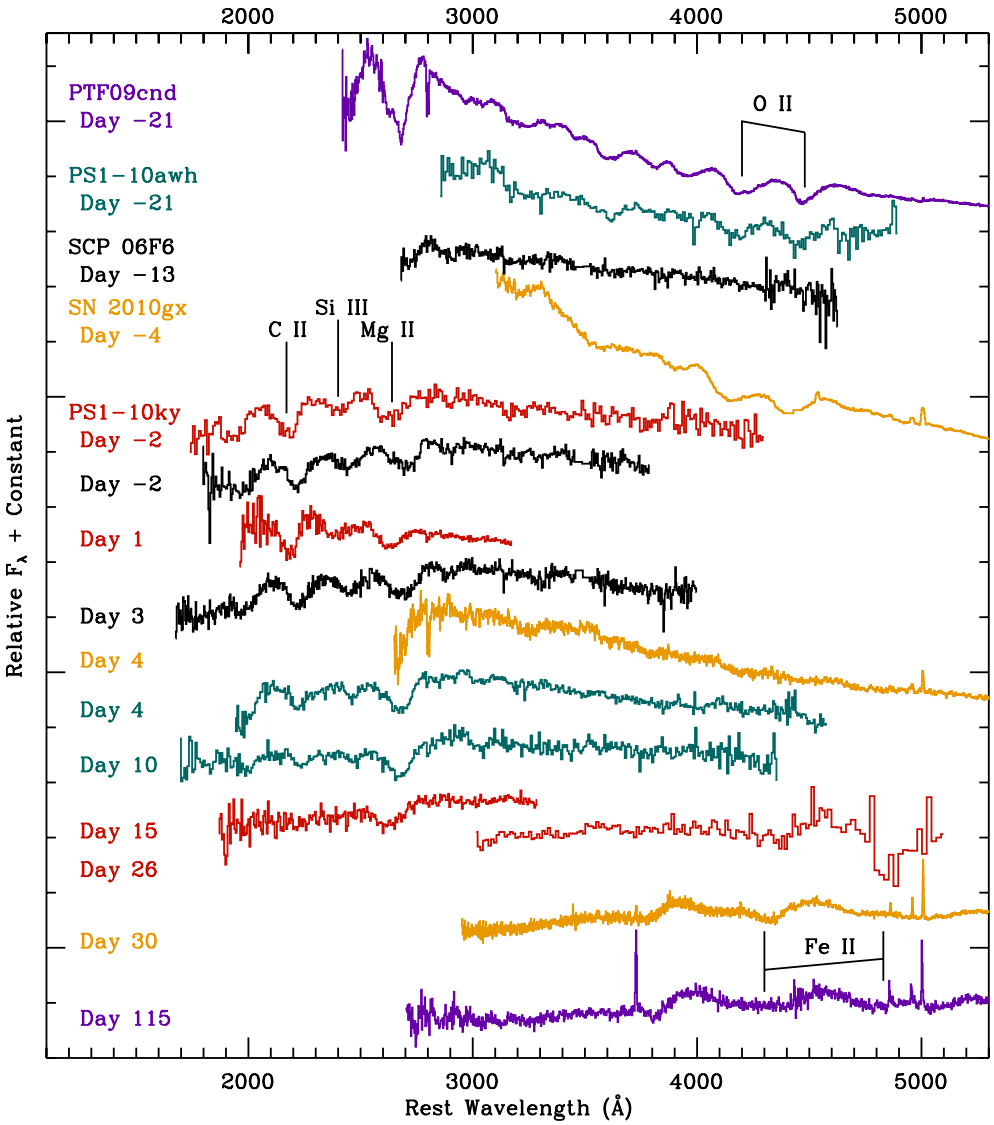

Figure 6. Spectra of PS1-10awh in blue, PS1-10ky in red, SN 2010gx (from Pastorello et al. 2010) in gold, SCP 06F6 (from Barbary et al. 2009) in black, and PTF09cnd (from Q+11) in violet. The time of each spectrum, relative to light curve peak in the rest frame, is marked on the left. Also marked are strong spectral features, tentatively identified as C II, O II, Si III, Mg II, and Fe II as discussed in the text.

5. BOLOMETRIC LUMINOSITY

To calculate the bolometric luminosities of these ultraluminous SNe, we used trapezoidal interpolation across all observed bands, and linearly extrapolated the integration out to the edges of the observed bands (most importantly, we impose a blue cutoff of 4050 Å to the g_{P1} band in the observer frame). We totaled up the interpolated flux for PS1-10awh between Days −21 and 10, and found an integrated energy of $(3.2 \pm 0.3) \times 10^{50}$ erg radiated during this time frame. Similarly for PS1-10ky, we constrained the bolometric luminosities between Days −3 and 43 and measured a radiated energy of $(3.8 \pm 0.6) \times 10^{50}$ erg. These are strong lower limits on the total radiated energy because they only represent the measured flux. Not all bands are constrained at all dates, and even when fluxes are constrained at all bands, we are only measuring the SED over a limited wavelength range (∼2100–5300 Å in the rest frame). Conveniently, the SEDs of SN 2005ap-like objects peak in the ultraviolet, around ∼2500 Å (e.g., Figures 6 and 7), so despite our limited rest-frame wavelength coverage, we may still be detecting the majority of the radiated energy.

Next, we attempt to more realistically model the bolometric luminosity by accounting for the flux emitted redward of the reddest band measured. The behavior of the SED blueward of the g_{P1} band is poorly understood and clearly diverges from a blackbody (Figure 7), but at redder wavelengths the spectrum can be roughly described as a Planck law. On any given date, we use the temperature measurements presented in the top panel of Figure 8 and splice the red tail of a blackbody curve of this temperature onto our measured SED. We then sum up the measured photometric points (as described above) with this blackbody tail. Bolometric light curves estimated using this technique are plotted in the middle panel of Figure 8. The bolometric light curves of PS1-10awh and PS1-10ky match up rather well, with maximum luminosities of $(2.4 \pm 0.2) \times 10^{44}$ erg s^{-1} and $(3.0 \pm 0.3) \times 10^{44}$ erg s^{-1}, respectively, translating to bolometric magnitudes of −22.2 and −22.5 mag. For SCP 06F6, we use the *i*- and *z*-band photometry published by Barbary et al. (2009) and blackbody tails with temperatures determined by the polynomial fit (black line in the top panel of Figure 8). Its light curve peaks at $(2.0 \pm 0.2) \times 10^{44}$ erg s^{-1}, but this is a lower limit due to lack of blue photometry

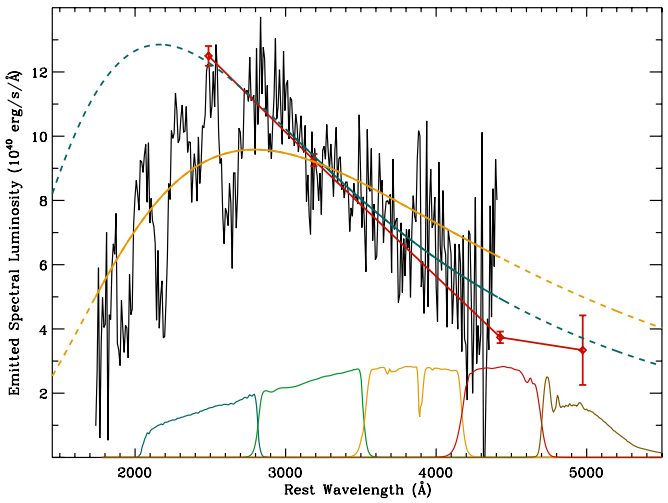

Figure 7. Spectrum of PS1-10ky observed at a phase of −2 days. Our PS1 photometry is overlain as red points connected with lines; the system response functions of the g_{P1}, r_{P1}, i_{P1}, z_{P1}, and y_{P1} filters are also shown at the bottom of the plot for reference. A blackbody fit to the full spectrum ($T = 10{,}400$ K) is shown as a solid gold line, and its extension to other wavelengths is represented by the gold dashed line. Similarly, the blackbody fit to the spectrum redward of 3000 Å ($T = 13{,}400$ K) is shown as a blue line.

Table 3
Spectroscopic Measurements

Date	Phase[a] (Days)	Temperature (K)	Velocity[b] (10^3 km s^{-1})	FWHM[c] (10^3 km s^{-1})
PS1-10ky				
2010 Jul 17	−2	13,400 ± 2700	19	12
2010 Jul 21	1	18,400 ± 9000	20	13
2010 Aug 18	15	9600 ± 4800	19	14
2010 Sep 9	26	7400 ± 1100	...	...
PS1-10awh				
2010 Oct 12	−21	18,100 ± 3600	15[d]	11[d]
2010 Nov 27	4	19,700 ± 3900	11	9
2010 Dec 9	10	10,200 ± 2000	11	9
SCP 06F6[e]				
2006 Apr 22	−13	19,800 ± 4000	...	...
2006 May 18	−2	13,000 ± 2600	12	12
2006 May 28	3	13,600 ± 1400	13	12
SN 2010gx[f]				
2010 Mar 22	−4	15,200 ± 800	19[d]	9[d]
2010 Apr 1	4	15,000 ± 2300	...	...
2010 Apr 9	10	12,900 ± 1900	19[g]	12[g]
2010 Apr 22	21	10,400 ± 1600	17[g]	16[g]
2010 May 2	30	6900 ± 1000	15[g]	9[g]
PTF09cnd[h]				
2009 Aug 25	−21	14,700 ± 1500	13[d]	9[d]
2010 Feb 11	115	6100 ± 1000	12[g]	...

Notes.
[a] In the rest frame.
[b] Velocity corresponding to line center for the three features in the blue (rest wavelengths of ∼2330, 2540, and 2800 Å) unless otherwise noted. Typical errors of ∼1000 km s^{-1}.
[c] Average FWHM for the three features in the blue, unless otherwise noted. Typical errors of ∼3000 km s^{-1}.
[d] This is a red spectrum, so velocities were measured from the O II "W" feature at ∼4300 Å.
[e] Spectra from Barbary et al. (2009).
[f] Spectra from Pastorello et al. (2010).
[g] Measured using the broad Fe II+Mg II feature around 4300 Å.
[h] Spectra from Q+11.

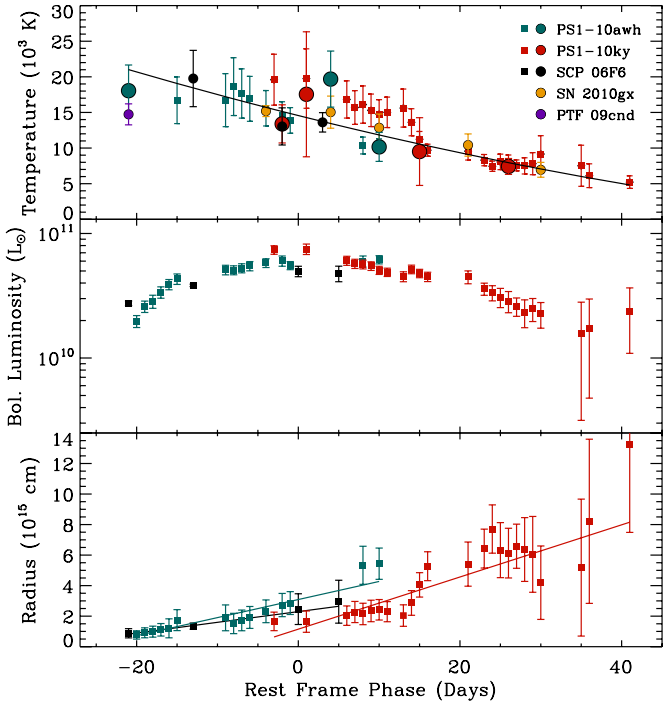

Figure 8. Top panel: temperature as a function of rest-frame time. Squares denote measurements from photometry, while circles are spectroscopic measurements. The quadratic fit to the PS1-10ky and PS1-10awh data is marked as a black solid line. Measurements for PS1-10awh are in blue, PS1-10ky in red, SCP 06F6 in black, SN 2010gx in gold, and PTF09cn in violet. Middle panel: bolometric luminosity as a function of time. These are determined by summing up flux in the measured photometric bands and extrapolating a blackbody tail to the red; emission blueward of 2100 Å (rest frame) for PS1-10ky/PS1-10awh and 3150 Å for SCP 06F6 is not accounted for, implying that these are lower limits. Bottom panel: radius as a function of time, assuming the bolometric luminosities from the middle panel and the temperatures from the top panel. Linear fits are marked by solid lines. In the middle and bottom panels, colors denote PS1-10ky, PS1-10awh, and SCP 06F6 as in the top panel.

to capture the peak of the SED (assuming a similar color evolution as PS1-10ky/PS1-10awh in the ultraviolet, we are likely underestimating its bolometric luminosity by a factor of ∼2). The bolometric light curves display slower declines than the single-band light curves (Figures 3 and 4), due to the cool temperatures at late times, which imply a larger correction from the red tail of the blackbody curve.

Using this technique, we find an integrated radiated energy of $(9.1 \pm 1.3) \times 10^{50}$ erg for the combined light curve of PS1-10ky and PS1-10awh, using PS1-10ky data before Day −3 and PS1-10awh data afterward. The radiated energies for the sources taken individually are $(5.3 \pm 0.5) \times 10^{50}$ erg for PS1-10ky between Days −21 and 10, and $(6.5 \pm 1.1) \times 10^{50}$ erg for PS1-10awh over the time range from Day −3 to 43. These are again likely to be lower limits, as we are not accounting for any flux blueward of 2100 Å and after Day 13, when the g_{P1}-band flux fades below detectability, we are not accounting for flux blueward of ∼2850 Å. Similarly, for SCP 06F6 we measure $(1.8 \pm 0.1) \times 10^{50}$ erg redward of 3150 Å and between Days −21 and 5 (after Day 5, the Barbary et al. detections are $<5\sigma$, and before Day −21, there are no constraints on the temperature evolution).

If we assume that these ultraluminous SNe can be described as blackbodies of the temperatures measured in Section 4 across their entire spectra (or alternatively, that the line-blanketed blue flux re-emerges at redder wavelengths, conserving the

Table 4
PS1 MDS + GALEX Photometry

UT Date	MJD	PS1-10ky							PS1-10awh						
		Phase[a] (days)	NUV (mag)	g_{P1} (mag)	r_{P1} (mag)	i_{P1} (mag)	z_{P1} (mag)	y_{P1} (mag)	Phase[a] (days)	NUV (mag)	g_{P1} (mag)	r_{P1} (mag)	i_{P1} (mag)	z_{P1} (mag)	y_{P1} (mag)
2010 Jun 26	55373.5	−12.0						21.23 ± 0.34	−74.0						>21.92
2010 Jul 11	55388.6	−4.3					21.39 ± 0.05		−66.1					>23.03	
2010 Jul 12	55389.5	−3.8		21.38 ± 0.03	21.13 ± 0.02				−65.6		>23.44	>23.59			
2010 Jul 21	55398.5	0.8		21.31 ± 0.10	21.11 ± 0.06				−60.9		>21.59	>22.20			
2010 Jul 23	55400.6	1.9					>21.57		−59.8					>21.09	
2010 Jul 25	55402.4	2.8						21.29 ± 0.36	−58.8						>21.28
2010 Jul 31	55408.5	5.9	>22.80			21.27 ± 0.05			−55.7				>22.60		
2010 Aug 1	55409.5	6.4	>22.70				21.38 ± 0.04		−55.1					>23.00	
2010 Aug 2	55410.5	6.9		22.06 ± 0.10	21.24 ± 0.05				−54.6		>22.63	>22.68			
2010 Aug 3	55411.5	7.5				21.47 ± 0.05			−54.1				>22.92		
2010 Aug 4	55412.5	7.9					21.29 ± 0.06		−53.6					>23.00	
2010 Aug 5	55413.4	8.4		21.99 ± 0.06	21.31 ± 0.03				−53.1		>23.25	>23.31			
2010 Aug 6	55414.5	9.0	>23.05			21.42 ± 0.03			−52.5	>23.05			>23.56		
2010 Aug 7	55415.6	9.5					21.46 ± 0.07		−51.9					>22.43	
2010 Aug 8	55416.5	10.0	>23.03	22.42 ± 0.08	21.40 ± 0.03				−51.5	>23.03	>23.50	>23.61			
2010 Aug 9	55417.5	10.5				21.44 ± 0.03			−50.9				>23.59		
2010 Aug 10	55418.8	11.2	>23.03						−50.2	>23.03					
2010 Aug 12	55420.6	12.1	>23.04						−49.3	>23.05					
2010 Aug 14	55422.5	13.1	>23.08	22.52 ± 0.16	21.51 ± 0.05				−48.3	>23.08	>23.24				
2010 Aug 15	55423.5	13.6				21.60 ± 0.03			−47.8				>23.31		
2010 Aug 16	55424.5	14.1	>23.11				21.67 ± 0.09		−47.3	>23.11				>23.18	
2010 Aug 17	55425.4	14.5		>22.83	21.75 ± 0.05				−46.8		>23.08	>22.92			
2010 Aug 18	55426.5	15.1	>23.03			21.62 ± 0.04			−46.2	>23.14			>23.17		
2010 Aug 19	55427.5	15.6					21.65 ± 0.05		−45.7					>23.25	
2010 Aug 20	55428.5	16.1	>22.99	>23.45	22.08 ± 0.08				−45.2	>23.15	>23.12	>23.24			
2010 Aug 22	55430.4	17.1	>23.02					21.59 ± 0.36	−44.2						>22.01
2010 Aug 28	55436.4	20.2					21.93 ± 0.11		−41.0					>22.70	
2010 Aug 29	55437.5	20.7		>22.33	21.95 ± 0.12				−40.5		>21.96	>22.36			
2010 Aug 30	55438.5	21.2				22.20 ± 0.07			−39.9				>23.21		
2010 Aug 31	55439.3	21.7					21.77 ± 0.05		−39.5					>23.17	
2010 Sep 1	55440.5								−38.9		>22.89	>22.71			
2010 Sep 2	55441.5	22.8				22.13 ± 0.05			−38.4				>23.06		
2010 Sep 3	55442.5	23.3					21.92 ± 0.08		−37.8					>22.72	
2010 Sep 4	55443.5	23.8	>23.02	>23.48	22.73 ± 0.12				−37.3		>23.31	>23.33			
2010 Sep 5	55444.4	24.3				22.38 ± 0.09			−36.8				>23.37		
2010 Sep 6	55445.4	24.8	>23.08				22.07 ± 0.10		−36.3					>23.16	
2010 Sep 7	55446.5	25.3		>23.06	22.69 ± 0.19				−35.7		>22.77	>22.72			
2010 Sep 8	55447.4	25.8				22.33 ± 0.05			−35.3				>23.59		
2010 Sep 9	55448.4	26.3					22.17 ± 0.08		−34.7					>23.26	
2010 Sep 10	55449.4	26.8		>23.43	22.99 ± 0.13				−34.2		>23.37	>23.45			
2010 Sep 11	55450.4	27.3				22.61 ± 0.10			−33.7				>23.34		
2010 Sep 12	55451.5	27.9					22.40 ± 0.18		−33.1					>22.61	
2010 Sep 13	55452.4	28.3		>23.43	23.22 ± 0.20				−32.7		>23.43	>23.26			

Table 4
(Continued)

UT Date	MJD	PS1-10ky							PS1-10awh						
		Phase[a] (days)	NUV (mag)	g_{P1} (mag)	r_{P1} (mag)	i_{P1} (mag)	z_{P1} (mag)	y_{P1} (mag)	Phase[a] (days)	NUV (mag)	g_{P1} (mag)	r_{P1} (mag)	i_{P1} (mag)	z_{P1} (mag)	y_{P1} (mag)
2010 Sep 14	55453.4	28.9				22.58 ± 0.06			−32.1				>23.62		
2010 Sep 15	55454.4	29.4					22.35 ± 0.10		−31.6					>23.15	
2010 Sep 16	55455.4	29.9		>23.11					−31.1		>22.85	>23.39			
2010 Sep 17	55456.4	30.4				22.58 ± 0.09			−30.6				>23.49		
2010 Sep 18	55457.3	30.9					22.57 ± 0.18		−30.1					>22.73	
2010 Sep 19	55458.3	31.4		>21.41	>22.12				−29.6		>21.38	>21.97			
2010 Sep 23	55462.4	33.5						>20.94	−27.4						>21.25
2010 Sep 24	55463.4	34.0						21.99 ± 0.38	−26.9						>21.94
2010 Sep 25	55464.4	34.5						>21.24	−26.3						>21.47
2010 Sep 26	55465.5	35.0				23.09 ± 0.19			−25.8				>22.62		
2010 Sep 27	55466.4	35.5					22.82 ± 0.17		−25.3					>22.85	
2010 Sep 28	55467.3	36.0		>22.93	>23.06				−24.8		>22.33	>23.03			
2010 Sep 29	55468.3	36.5				23.27 ± 0.16			−24.3				>23.25		
2010 Oct 4	55473.3	39.0		>23.09	>23.32				−21.7		22.91 ± 0.17	22.75 ± 0.12			
2010 Oct 6	55475.2	40.0					22.55 ± 0.17		−20.7					>22.92	
2010 Oct 8	55477.2	41.0				23.18 ± 0.10			−19.6				22.33 ± 0.08		
2010 Oct 9	55478.2	41.6					22.72 ± 0.15		−19.1					22.52 ± 0.14	
2010 Oct 10	55479.2	42.1		>23.06	>23.26				−18.6		22.08 ± 0.10	22.09 ± 0.10			
2010 Oct 11	55480.2	42.6				>23.21			−18.1				22.17 ± 0.15		
2010 Oct 12	55481.2	43.1					>22.70		−17.6					>22.31	
2010 Oct 13	55482.2	43.6		>23.14	>23.15				−17.0		21.83 ± 0.09	21.75 ± 0.06			
2010 Oct 14	55483.2	44.1				23.60 ± 0.15			−16.5				21.94 ± 0.05		
2010 Oct 15	55484.2	44.6					>23.00		−16.0					21.94 ± 0.10	
2010 Oct 17	55486.3	45.7				>22.65			−14.9				21.66 ± 0.12		
2010 Oct 23	55492.3	48.8						>21.23	−11.7						23.01 ± 0.00
2010 Oct 24	55493.3	49.2						21.81 ± 0.39	−11.2						21.78 ± 0.20
2010 Oct 27	55496.3	50.8					>22.24		−9.7					21.58 ± 0.13	
2010 Oct 29	55498.2	51.8				>23.66			−8.6				21.50 ± 0.04		
2010 Oct 30	55499.2	52.3					>22.58		−8.1					21.64 ± 0.08	
2010 Oct 31	55500.2	52.8		>23.14	>23.32				−7.6		21.53 ± 0.05	21.39 ± 0.05			
2010 Nov 1	55501.4	53.4				>23.36			−7.0				21.50 ± 0.07		
2010 Nov 2	55502.3	53.8					22.95 ± 0.21		−6.5					21.55 ± 0.07	
2010 Nov 3	55503.3	54.4		>23.45	>23.30				−6.0		21.48 ± 0.06	21.35 ± 0.05			
2010 Nov 7	55507.3	56.4				>23.47			−3.9				21.28 ± 0.04		
2010 Nov 8	55508.2	56.9					>22.49		−3.4					21.47 ± 0.07	
2010 Nov 10	55510.2	57.9				>23.77			−2.3				21.17 ± 0.02		
2010 Nov 12	55512.3	59.0		>22.28					−1.3		21.51 ± 0.15				
2010 Nov 23	55523.3	64.6						>21.55	4.5						21.64 ± 0.19
2010 Nov 30	55530.2	68.1		>22.54	>22.56				8.1		>22.24	21.52 ± 0.12			
2010 Dec 4	55534.3	70.2				>23.39			10.2				21.23 ± 0.06		
2010 Dec 5	55535.2	70.7					>22.82		10.7					21.21 ± 0.05	
2010 Dec 6	55536.2	71.2		>22.83	>23.21				11.3			21.45 ± 0.05			
2010 Dec 17	55547.2	76.8					>23.01		17.0					21.61 ± 0.06	

Table 4
(Continued)

UT Date	MJD	PS1-10ky							PS1-10awh						
		Phase[a] (days)	NUV (mag)	g_{P1} (mag)	r_{P1} (mag)	i_{P1} (mag)	z_{P1} (mag)	y_{P1} (mag)	Phase[a] (days)	NUV (mag)	g_{P1} (mag)	r_{P1} (mag)	i_{P1} (mag)	z_{P1} (mag)	y_{P1} (mag)
2011 Jun 26	55738.6	174.7				>23.17			117.3				>22.71		
2011 Jun 27	55739.5	175.1					>22.59		117.8					>22.70	
2011 Jun 29	55741.6	176.2				>23.57			118.9				>23.26		
2011 Jun 30	55742.6	176.7					>23.62		119.4					>23.35	
2011 Jul 1	55743.6	177.2		>23.60	>23.11				119.9		>23.34	>23.13			
2011 Jul 5	55747.6	179.3				>23.56			122.0				>23.27		
2011 Jul 9	55751.6	181.3					>23.13		124.1					>23.31	
2011 Jul 12	55754.6	182.8					>22.81		125.7					>22.80	
2011 Jul 13	55755.6	183.4						>21.92	126.2						>22.10
2011 Jul 14	55756.6	183.9						>21.81	126.7						>21.76
2011 Jul 15	55757.5	184.3						>21.19	127.2						>21.93
2011 Jul 21	55763.6	187.5					>22.08		130.4					>22.17	>20.69
2011 Jul 22	55764.6	188.0		>22.85	>23.22				130.9		>22.60	>22.99			
2011 Jul 23	55765.6	188.5				>23.35			131.4				>22.89		

Note.
[a] In days relative to peak brightness, corrected for time dilation.

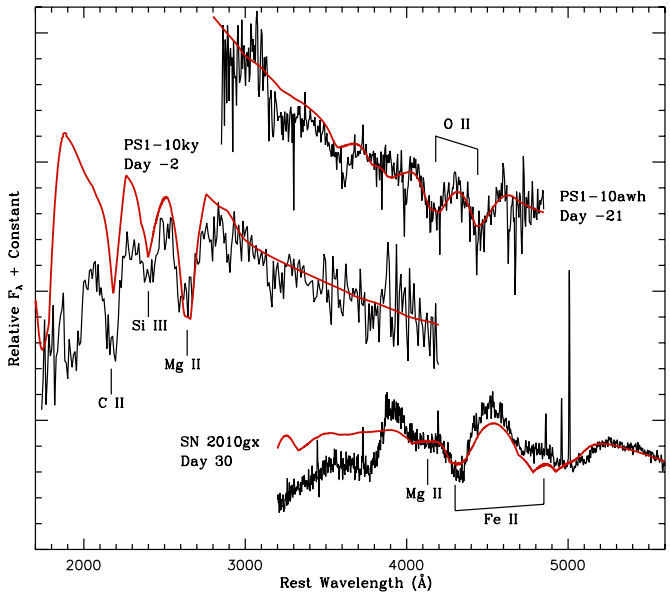

Figure 9. SYNOW fits to three spectra are marked as red lines overlying the spectra. The top spectrum is of PS1-10awh on Day −21, and was fit with O II. The middle spectrum is of PS1-10ky on Day −2 and shows the characteristic blue triplet of lines, fit with C II, Si III, and Mg II. The bottom spectrum is SN 2010gx on Day 30 and is fit with Fe II and Mg II.

(A color version of this figure is available in the online journal.)

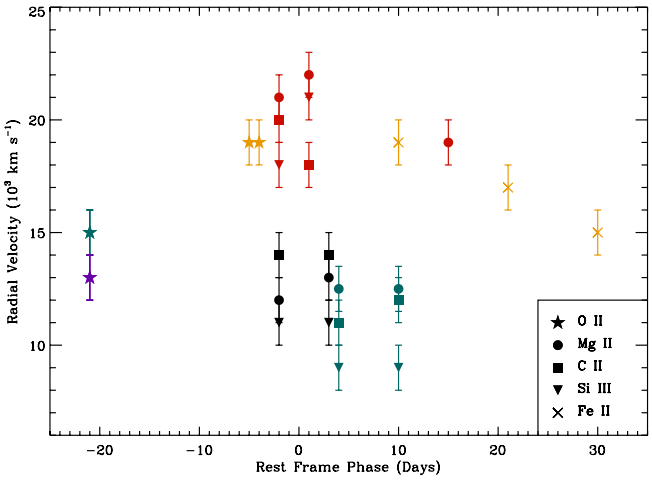

Figure 10. Radial velocities measured from absorption lines as a function of rest-frame time relative to light curve maximum. Measurements for PS1-10awh are in blue, PS1-10ky in red, SCP 06F6 in black, SN 2010gx in gold, and PTF09cnd in violet. Different absorption lines are denoted by a variety of symbols, as shown in the key at lower right.

(A color version of this figure is available in the online journal.)

blackbody luminosity), the estimate of the total radiated energy increases to $(1.4 \pm 0.4) \times 10^{51}$ erg for PS1-10ky/PS1-10awh and $(1.1 \pm 0.2) \times 10^{51}$ erg for SCP 06F6. These can essentially be viewed as upper limits on the radiated energy over the time ranges constrained by observations.

6. EXPANSION VELOCITY

We can constrain the expansion velocity of PS1-10ky, PS1-10awh, and SCP 06F6 by measuring the blueshift of the absorption lines, assuming that their rest frame coincides with the narrow Mg II absorption seen in their spectra (presumably from the host galaxy), and that the lines are identified correctly by Q+11. For spectra with coverage in the blue, we modeled C II, Si II, and Mg II in SYNOW (Jeffery & Branch 1990), with lines formed at an excitation temperature of 10,000 K, a radial power-law distribution of line optical depth proportional to r^{-7}, and a maximum ejecta velocity of 40,000 km s^{-1}. A typical fit is shown as the middle spectrum in Figure 9; the simple SYNOW fit does not fully treat the continuum and significantly diverges from the observed continuum in the blue, but the absorption features are roughly reproduced. The central wavelength of each absorption feature is primarily determined by the SYNOW parameter vmine, which signifies the lowest velocity at which a given ion is present in the ejecta. In all cases, values of vmine for C II, Si II, and Mg II agree within 4000 km s^{-1} (Figure 10), and we set the photospheric velocity to the lowest value of vmine found between these three ions. For the expansion velocities quoted in Table 3, we take the average of the three values of vmine. We find expansion velocities measured at absorption minima of ∼19,000 km s^{-1} for PS1-10ky and ∼12,000 km s^{-1} for PS1-10awh and SCP 06F6 (Table 3). A glance at Figure 6 confirms that PS1-10ky is indeed expanding faster than the other two SNe—the three absorption features between 2000 and 3000 Å are noticeably bluer for this source.

For the Day −21 spectrum of PS1-10awh with redder wavelength coverage, we similarly fit the O II "W"-shaped feature in SYNOW, making the same assumptions as above except using an excitation temperature of 13,000 K (Figure 9). We find an expansion velocity of ∼15,000 km s^{-1}. The spectrum of SCP 06F6 from 2006 April 22 and the spectrum of PS1-10ky from 2010 September 9 could not be evaluated, as there are no clear spectral features present (we note that there are no apparent O II features in the SCP 06F6 spectrum from Day −13, while they are clear in the first spectrum of PS1-10awh from Day −21 and the SN 2010gx spectra from Day −5 and Day −4).

As a simple diagnostic of line shape, we also fit the FWHM of each line and take the average if there are multiple features measured in a spectrum; these are also listed in Table 3. This is certainly an oversimplistic interpretation of the line shapes, as some of the features are blends and therefore they will not necessarily have the same width or structure. Typical spreads in our measurement of FWHM are large, on the order of 3000 km s^{-1}. Line widths are typically 9000–12,000 km s^{-1}.

PS1-10awh, PS1-10ky, and SCP 06F6 show no evidence for decreasing line velocity with time, displaying similar expansion velocities before and after light curve peak (Table 3 and Figure 10). This is roughly consistent with the bottom panel of Figure 8, where we plot the estimated radii as a function of time, assuming effective temperatures measured as described in Section 4 (except in the case of SCP 06F6, where we use the quadratic fit to temperature as a function of time) and luminosities determined from the technique which accounts for photometric flux and the red blackbody tail, described in Section 5. The estimates of radius are very noisy, but growth with time can be fit with a straight line for these three sources, as would be expected for a roughly constant photospheric velocity. The best-fit expansion velocities of the blackbody photospheres are 13,700 ± 2200 km s^{-1} for PS1-10awh, 19,800 ± 2900 km s^{-1} for PS1-10ky, and 8100 ± 3800 km s^{-1} for SCP 06F6. Given the large uncertainties, these velocities measured from radius estimates are consistent with our measurements from the spectral lines.

Finally, we briefly note that SN 2010gx, during its later phase when its spectrum shows SN Ic-like features, displays signs of

decreasing photospheric velocity. Using the spectra observed on Days 10, 21, and 30 (Pastorello et al. 2010), we fit the broad absorption feature around 4300 Å in SYNOW, describing it with a blend of Fe II and Mg II and assuming basic parameters as described above (bottom spectrum in Figure 9). The feature is observed to decrease in velocity, from 19,000 km s^{-1} on Day 10 to 17,000 km s^{-1} on Day 21 and then to 15,000 km s^{-1} on Day 30.

Our analysis for these ultraluminous SNe implies that while they show SN 2005ap-like features in their spectra, they do not display any clear sign of change in the rate of photospheric expansion. This apparent lack of deceleration is in contrast with SN 2005ap, where the "W"-shaped feature is observed to decelerate by 4000 km s^{-1} over seven days in the rest frame (Quimby et al. 2007). However, the apparently constant velocities measured for PS1-10ky, PS1-10awh, and SCP 06F6 are mostly measured from the blue lines of C II, Mg II, and Si III and it is possible that these lines form at a significantly different location in the photosphere from the O II "W"-shaped feature; therefore, perhaps it is not surprising that they show different velocity evolution. Late-time spectroscopy on SN 2010gx hints that, later in the evolution of these ultraluminous SNe, the measured velocities may decline as typically observed during the photospheric phase of SN expansion, while the photosphere recedes into progressively slower-moving ejecta.

7. MODELS FOR SN 2005ap-LIKE SNe

In this section, we consider three physical scenarios that have been proposed to explain ultraluminous SNe. We compare the predictions of these models with the data presented above, in an effort to define the parameter space that these objects may inhabit. When we discuss bolometric light curves, we are using the luminosities calculated by totaling up the flux in the observed bands and adding on the red tail of a blackbody fit, as described in Section 5 and plotted in Figure 8. These are likely to be slight underestimates of the true bolometric luminosity for PS1-10awh and PS1-10ky, but they are the best estimate we can make given our limited wavelength coverage.

7.1. Scenario 1: Radioactive Decay

Free from the H-envelopes associated with most Type II SNe, the photospheric emission from Type I SNe is powered by the radioactive decay of freshly synthesized ^{56}Ni and ^{56}Co within the ejecta. The associated optical signal reaches maximum intensity within a month of the explosion at which point the photons diffuse efficiently out of the optically thick layers causing the light curve to decay. The characteristic time of photon diffusion, $\tau_c \propto M_{\rm ej}^{3/4} E_K^{-1/4}$ days, is determined by fundamental ejecta properties (Arnett 1982): the total mass ($M_{\rm ej}$) and the kinetic energy (E_K). Simple analytical models for Type I SN light curves assume homologous expansion, a uniform density profile, constant opacity, and the diffusion approximation for photons.

As originally shown by Phillips (1993) for Type Ia SNe and Valenti et al. (2008) and Drout et al. (2010) for SNe Ibc, the post-maximum decay rate may serve as a proxy for the light curve width since broader light curves are associated with slower decline rates. We adopt the notation, Δm_{15}, which represents the magnitude decrease in the 15 days following the peak luminosity. The peak luminosity ($L_{\rm peak}$) is primarily determined by the mass of ^{56}Ni ($M_{\rm Ni}$; see Arnett 1982). Meanwhile, spectroscopic measurements of the photospheric velocity ($v_{\rm ph}$) directly constrain the quantity $\sqrt{E_K/M_{\rm ej}}$, thus enabling all three physical parameters ($M_{\rm Ni}$, E_K, and $M_{\rm ej}$) to be determined uniquely based on three observables: (1) the peak luminosity, (2) the light curve width, and (3) the velocity of the photosphere.

For the rest-frame light curve of PS1-10ky, we measure a peak bolometric luminosity of $L_{\rm peak} \approx 3.0 \times 10^{44}$ erg s^{-1} and a post-maximum decay rate of $\Delta m_{15} \approx 0.5$ mag. Assuming that SN 2005ap-like objects are simply scaled-up SNe Ibc undergoing homologous expansion, and using theoretical models for Type Ic SN light curves (Valenti et al. 2008), this decay rate implies a characteristic time of $\tau_c \approx 14$ days and a radioactive mass of $M_{\rm Ni} \approx 14\,M_\odot$. With the photospheric velocity of $v_{\rm ph} \approx 19{,}000\,{\rm km\,s^{-1}}$ measured for PS1-10ky, we estimate $M_{\rm ej} \approx 4.7\,M_\odot$ and $E_K \approx 1.1 \times 10^{52}$ erg. This ejecta mass is much less than the nickel mass, implying that this simple model where radioactive decay powers the bulk of the light curve is unphysical. This is consistent with the findings of Chatzopoulos et al. (2009) and Q+11.

However, our measurements of photospheric velocity presented in Section 6 hint that perhaps SN 2005ap-like sources are not in homologous expansion. Their relatively constant photospheric velocities may be more consistent with an optically thick shell, with a significant amount of mass expanding at a discrete velocity. This shell-like morphology is predicted by both the magnetar (Section 7.2) and circumstellar interaction (Section 7.3) scenarios, but would invalidate the assumptions of the radioactive decay model discussed here. However, in order to sweep up the majority of the SN ejecta into a shell, an engine (like a magnetar) would be required that itself rivals or exceeds the energy in the SN, and would undoubtedly alter the resulting light curve significantly. Therefore, an SN with its ejecta swept into a shell is unlikely to be primarily powered by radioactive decay.

At later epochs and when the ejecta are optically thin ($\Delta t \approx$ 60–300 days), energy generation within a normal SN's ejecta is dominated by the radioactive decay of ^{56}Co (half-life $\tau =$ 77 days, corresponding to a decay of $\sim$0.01 mag day^{-1}). Late-time light curves can thus directly probe the mass of radioactive decay products, enabling an independent constraint on $M_{\rm Ni}$. The appearance of SN 2010gx and PTF09cnd as SNe Ic at late times implies that such an extended slowly decaying tail should appear in the light curves of SN 2005ap-like objects at a low level, if we observe deeply enough and at late enough times. Q+11 constrain the photometric evolution of three SN 2005ap-like sources $\sim$100–150 rest-frame days after light curve maximum, and they find that the light curves, even at these relatively late times, decline too steeply to be powered by radioactive decay. Photometric constraints on SN 2010gx from 76 days after light curve peak place limits on the ^{56}Ni mass ejected by SN 2010gx of $\lesssim 1\ M_\odot$ (Pastorello et al. 2010). Late-time observations of PS1-10ky on 2011 June 29 (Day 176) imply a 5σ $i_{\rm P1}$-band limit of $>$23.6 mag, corresponding to a weak constraint on the nickel mass of $M_{\rm Ni} \lesssim 41\ M_\odot$ (assuming some gamma-ray leakage). Additional very late observations of SN 2005ap-like objects (hundreds of days after explosion in the rest frame) are needed to place further constraints on $M_{\rm Ni}$ in these systems.

7.2. Scenario 2: Magnetar Spin-down

Kasen & Bildsten (2010, henceforth KB10) and Woosley (2010) have shown that the spin-down of a magnetar can explain the ultraluminous SNe with broader light curves and slower

decays like SN 2005ap (Quimby et al. 2007) and SN 2008es (Gezari et al. 2009; Miller et al. 2009). However, it remains unclear if they can fit the relatively narrow symmetric light curves of the SN 2005ap-like objects presented here. We use the formalism of KB10 to model SN light curves powered by magnetar spin-down. The magnetar has a rotational energy $E_p = 2 \times 10^{50}\ P_{10}^{-2}$ erg, where P_{10} is its period in units of 10 ms (maximal spin corresponds to ~1 ms). The spin-down timescale due to magnetic dipole radiation is $t_p = 1.3\ B_{14}^{-2}\ P_{10}^{2}$ yr, where B_{14} is the magnetar magnetic field strength in units of 10^{14} G. It spins down as $L_p(t) = [E_p(l-1)]/[t_p(1+t/t_p)^l]$, where t is the time since birth, L_p is the energy the magnetar is depositing into the SN ejecta per unit time, and l is an index that describes the magnetar spin-down ($l = 2$ for magnetic dipole spin-down). The velocity of the SN ejecta is $v_{\rm ej} = [2(E_p + E_{\rm SN})/M_{\rm ej}]^{1/2}$, where $E_{\rm SN}$ is the SN explosion energy and $M_{\rm ej}$ is the SN ejecta mass. Finally, the diffusion timescale is $t_d = [(3M_{\rm ej}\kappa)/(4\pi v_{\rm ej} c)]^{1/2}$, where κ is the opacity in cm^2 g^{-1} and c is the speed of light.

Using these definitions, we solve for the emitted luminosity L_e with the differential equation

$$\frac{\partial L_e(t)}{\partial t} = \frac{E_p(l-1)t}{t_d^2 t_p(1+t/t_p)^l} - \frac{t\ L_e(t)}{t_d^2} \quad (1)$$

and then multiply the luminosity by a correction factor $(l + 1)/2$ as prescribed by KB10. Using this simple technique, the time to peak luminosity also differs from that solved for in hydrodynamic simulations by KB10. We use their Equation (16) to solve for the "correct" peak time, and then scale the time axis of our light curve so that the peak time produced by our Equation (1) matches it. We find that we can match the published light curves in KB10 well with these simple assumptions.

We leave fixed $l = 2$, $\kappa = 0.2$ cm^2 g^{-1} (as assumed by KB10), and $E_{\rm SN} = 10^{51}$ erg; we vary P_{10}, B_{14}, and $M_{\rm ej}$. The combined bolometric light curve for PS1-10awh and PS1-10ky can be matched reasonably well with $B_{14} = 3.0$, $P_{10} = 0.12$, and $M_{\rm ej} = 5\ M_\odot$, represented as the solid line in Figure 11. We recognize that the light curves for PS1-10awh and PS1-10ky do not match up perfectly, so PS1-10awh is only used as a rough constraint on the rise time. The magnetar in such a model dominates the SN energy with a rotational energy of 1.4×10^{52} erg, and the swept-up shell will expand at 17,300 km s^{-1}, also in good accord with measured expansion velocities.

We can also perform a rough comparison with our observed temperature evolution by calculating the effective temperatures of the magnetar models $T = [L_e/(4\pi\sigma v_{\rm ej}^2 t^2)]^{1/4}$, where σ is the Stefan–Boltzmann constant. We plot the predicted temperature evolution in the bottom panel of Figure 11, and find that it is consistent with our data (however, it should be noted that a detailed comparison of the temperature evolution at early times really requires a full hydrodynamic treatment as in KB10, where they predict that the temperature will rise at early times, and then turn over around light curve peak and approach our approximation in Figure 11).

The combined light curve can be fit with a range of ejecta masses, from 4 to 6 $M_\odot$. For lower ejecta masses, P_{10} must increase and B_{14} must decrease to fit the data. For example, the best match for $M_{\rm ej} = 4\ M_\odot$ is $B_{14} = 2.6$ and $P_{10} = 0.16$ (implying an expansion velocity of 14,900 km s^{-1}), while for $M_{\rm ej} = 6\ M_\odot$ the data can be described well with $B_{14} = 3.2$, $P_{10} = 0.10$ (giving a velocity of 18,800 km s^{-1}). The range

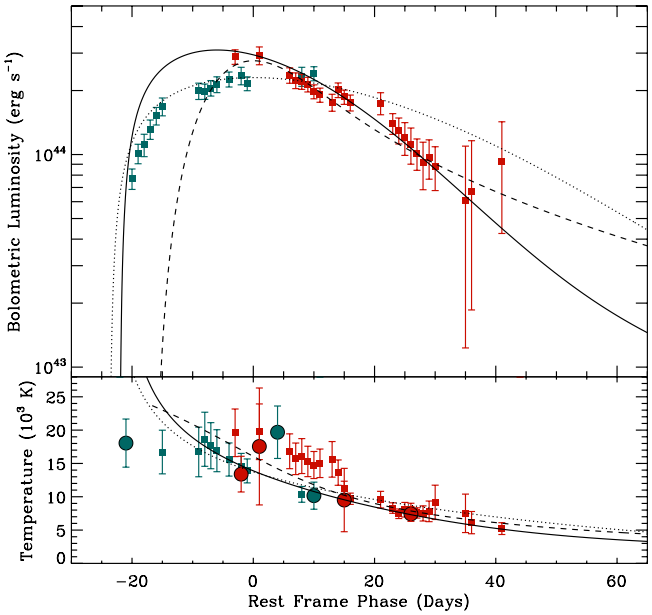

Figure 11. Top panel: combined bolometric light curve for PS1-10awh and PS1-10ky (colors and symbols as in Figure 8) fit using magnetar spin-down models (Kasen & Bildsten 2010). Different lines correspond to fits for different SN ejecta masses: $M_{\rm ej} = 1\ M_\odot$ (dashed; $B_{14} = 1.3$, $P_{10} = 0.34$), $5\ M_\odot$ (solid; $B_{14} = 3.0$, $P_{10} = 0.12$), and $10\ M_\odot$ (dotted; $B_{14} = 2.4$, $P_{10} = 0.1$). Bottom panel: temperature evolution plotted as in Figure 8, with the effective temperature of the magnetar spin-down models overplotted as lines as in the top panel.

(A color version of this figure is available in the online journal.)

of ejecta masses that fit the combined light curve is limited, as illustrated by two additional models in Figure 11. The dotted line shows a light curve that matches the PS1-10awh rise of the light curve for $M_{\rm ej} = 10\ M_\odot$; clearly the late-time decline of the light curve is too gradual to match what is observed for PS1-10ky. This lack of good fit for high $M_{\rm ej}$ is due to the maximal spin of a magnetar at $P_{10} = 0.1$ (KB10). There is also no good fit to the combined light curve for $M_{\rm ej} = 1\ M_\odot$ (dashed line), as a model that produces peak luminosity and light curve decline to match PS1-10ky also predicts a light curve rise that is far too rapid to match PS1-10awh (although we note that such a rapid rise is reminiscent of SN 2010gx). However, a complete bolometric light curve of an SN 2005ap-like object is needed to conclusively constrain the possible range of ejecta masses. If we consider PS1-10ky and PS1-10awh separately, the plausible range of ejecta masses is broader, although we can still rule out $M_{\rm ej} > 8\ M_\odot$ for PS1-10ky (consistent with ejecta masses for SNe Ibc, typically $< 5\ M_\odot$; Drout et al. 2010). In the magnetar model, different ejecta masses would explain the measured differences in expansion velocity.

The KB10 magnetar model also makes the distinct prediction that the SN photospheric velocity should be constant with time, consistent with our observations (Section 2.2). This is because the magnetar blows a hot low-density bubble in the center of the SN, producing a dense fast-moving shell that sweeps up the ejecta. Unlike in a normal SN, where the photosphere recedes inward to ejecta with slower velocities, the photosphere stalls at this dense shell in the magnetar model, implying a roughly constant observed expansion velocity. However, it is possible that the magnetar spin-down model would struggle to produce late-time SN Ic emission as seen in SN 2010gx, for this very same reason: the magnetar has cleared out a low-density bubble around it, and the ejecta are no longer expanding homologously

but as a relatively thin shell. We also note that the measured evolution of the radius (Figure 8) is consistent with a shell that begins expanding at constant velocity from a very small radius around Day −40 or Day −30, roughly coincident with the first detections of SN 2005ap-like sources; however, our radius calculations are very uncertain, and better temperature determinations before light curve maximum are required to constrain the radius at early times.

7.3. Scenario 3: Shock Breakout and Circumstellar Interaction

The extremely high radiated energies of many ultraluminous SNe has been explained by interaction with a dense circumstellar medium (CSM). The general idea is that interaction with CSM transforms much of the SN's kinetic energy into radiation before it can be lost to adiabatic expansion (e.g., Smith & McCray 2007; Chevalier & Irwin 2011).

Chevalier & Irwin (2011, henceforth CI11) propose that the light curves of SN 2005ap-like objects might be explained by shock breakout from a dense but truncated CSM. A stellar wind with mass loss rate $\dot{M}$ and velocity v_w is expelled from the SN progenitor for a time $t_{\rm ml}$ before the SN explosion, producing a $\rho \propto r^{-2}$ density profile that abruptly drops to zero for radii greater than $r_w = t_{\rm ml} v_w$. If the diffusion radius of the SN (r_d) is roughly equivalent to the radius of this stellar wind, SN energy will be transformed into radiation very efficiently, resulting in a luminous burst of radiation with a fairly symmetric light curve. We can use our measured peak bolometric luminosity ($L_{\rm peak} \approx 3 \times 10^{44}$ erg s^{-1}) and peak temperature ($T_{\rm peak} \approx$ 15,000 K) to measure this radius ($r_w \approx 2.9 \times 10^{15}$ cm). From the PS1-10awh light curve, we estimate a rise time of $t_d \approx 25$ days, which can be roughly equated to the diffusion time t_d:

$$t_d = 6.6\, k\, D_\star \text{ days}, \quad (2)$$

where k is the opacity in units of 0.34 cm^2 g^{-1} and $D_\star$ parameterizes the mass loss in the stellar wind as $D_\star = (\dot{M}/10^{-2}\ M_\odot)(v_w/10\ \text{kms}^{-1})$. For an ionized He-rich wind, $k = 0.59$ and we find $D_\star = 6.4$. Integrating this density profile out to r_w, we find that the total mass in the stellar wind is 5.8 $M_\odot$. Assuming a Wolf–Rayet (W-R) progenitor star with v_w = 1000 km s^{-1} (Nugis & Lamers 2000), this corresponds to a wind powered for approximately one year at a mass loss rate $\dot{M} \approx 6\ M_\odot$ yr^{-1}.

Such a mass loss event, expelling several solar masses in the year before stellar death, is extreme, although such episodes are seen for luminous blue variables (LBVs; e.g., Davidson & Humphreys 1997; Smith & Owocki 2006). Pastorello et al. (2007) discovered such an outburst preceding the Type Ib SN 2006jc by two years; they attempt to reconcile the LBV-like outburst with the W-R progenitor of the SN, but point out that no such outburst has ever been observed for a W-R star. They conclude that perhaps the W-R progenitor is in a binary with an LBV, or perhaps such outbursts on W-R stars are exceedingly rare. Meanwhile, Foley et al. (2007) point out that a dense He-rich CSM is required to explain the bright He I emission lines in SNe 1999cq, 2002ao, and 2006jc, and hypothesize that perhaps LBV-like eruptions can persist into the W-R stage. However, X-ray measurements of SN 2006jc imply that the CSM may not be particularly massive (of order 0.01 $M_\odot$; Immler et al. 2008), and therefore an episode like that seen in SN 2006jc would need to be significantly scaled up to explain SN 2005ap-like sources.

Given the integrated radiated energy of our combined light curve ($E_{\rm rad} = 9.1 \times 10^{50}$ erg) and k and $D_\star$ as described above, we can use Equation (5) from CI11 to find that $E_{51}^2/M_{\rm ej,10} = 19$, where E_{51} is in units of 10^{51} erg and $M_{\rm ej,10}$ is in units of 10 $M_\odot$. For an ejecta mass of 10 $M_\odot$, this implies an SN energy of 4.3×10^{51} erg. We can also solve for the diffusion radius using Equation (3) from CI11 and find $r_d = 1.4 \times 10^{15}$ cm, similar to r_w within a factor of two and implying that these objects are in the $r_w \approx r_d$ regime where radiation is produced most efficiently.

The inner ejecta of an SN explosion typically have a rather flat density profile ($\rho_{\rm in} \propto r^{-1}$ or constant), while the density of the outermost ejecta falls off much more steeply ($\rho_{\rm out} \propto r^{-7}$). The CI11 model assumes that the reverse shock is evolving into the steep outer part of the density profile, but this is only true if $E_{51}^{0.5}\ M_{\rm ej,10}^{-1.5}\ D_\star\ t_{\rm SN} < 320$, where $t_{\rm SN}$ is the age of the SN in days. At the beginning of shock breakout, $t_{\rm SN} = t_d$ and this condition is marginally satisfied for an ejecta mass of 10 $M_\odot$. As shock breakout proceeds, the reverse shock will proceed toward the flatter part of the density profile. For ejecta masses smaller than 10 $M_\odot$, $E_{51}^{0.5}\ M_{\rm ej,10}^{-1.5}\ D_\star\ t_{\rm SN} > 320$ at t_d, and a model for circumstellar interaction will be required that takes into account both the $\rho_{\rm out}$ and $\rho_{\rm in}$ regimes of the ejecta density profile (however, the development of such a model is outside the scope of this present work).

The energy in the swept-up shell is 3.1 $E_{\rm rad}$, where $E_{\rm rad}$ is the internal energy in the shell, which is dominated by radiation and will be released upon breakout. The velocity of the shell can be estimated using Equation (4) of CI11 as

$$v\ (\text{km s}^{-1}) = 6.9 \times 10^{-13} \sqrt{E_{\rm rad}^{2/3}\ k^{2/3}\ t_d^{-4/3}} \quad (3)$$

implying that the velocity, in this model, is a simple function of the radiated energy and the rise time of the light curve (and our assumptions about opacity). For PS1-10ky/PS1-10awh, this corresponds to a shell velocity of 6600 km s^{-1}, which is lower than we observe. Increasing $E_{\rm rad}$ or decreasing t_d could bring the predicted velocity in better line with the measurements, but is unlikely to be sufficient to match the measured photospheric velocities. For example, the rise time, and therefore t_d, is not constrained for PS1-10ky, and it might be smaller than 25 days, but in this case it is difficult to avoid an associated decrease in $E_{\rm rad}$. If we leave t_d at the 25 days measured for PS1-10awh and increase $E_{\rm rad}$ to 1.4×10^{51} erg, the velocity only increases to 7600 km s^{-1}. It would be possible to further increase the velocity if the high-density CSM is concentrated in a toroidal region while the high-velocity material expands away from this dense region.

In a related scenario, Metzger (2010) suggests that the dense CSM might actually be a residual massive protostellar disk surrounding the SN progenitor star. Although such a disk would be H-rich, Metzger claims that if it is compact and dense enough, it will be engulfed by the optically thick SN ejecta before it can radiate and show signatures of H. To retain such a disk through the entire lifetime of a massive star would require extraordinary circumstances—likely the star would need to be in an unusually quiescent and low-metallicity environment. In addition, for plausible protostellar disk parameters, the radiative efficiency is unlikely to exceed 10%, implying that an unusually energetic SN would still be required within this model to explain the class of SN 2005ap-like transients (B. Metzger 2011, private communication).

Smith & McCray (2007) propose a scenario similar to CI11 to explain the light curve of SN 2006gy. However, in their model the SN shock does not break out of an r^{-2} smooth wind, but

rather plows into an optically thick shell. The exact density profile of the CSM will not change the light curve significantly, as the light curve is largely determined by simply the radius and mass of the surrounding material. Therefore, the Smith & McCray model gives results similar to those derived above using CI11.

The same basic physics also operates in the pulsational pair-instability model (Woosley et al. 2007). In this scenario, a massive star has not yet exploded and died, but in approaching the end of its life violently ejects massive shells (some as massive as 18 $M_{\odot}$) that collide with one another and produce luminous outbursts. Some of the theoretical light curves feature rather steep declines reminiscent of the SN 2005ap-like sources. However, the Woosley et al. (2007) model struggles to produce outbursts with velocities significantly in excess of ∼5000 km s^{-1}, even for a massive progenitor star of 130 $M_{\odot}$. We therefore find pulsational pair-instability SNe to be an unlikely model for SN 2005ap-like objects. We also note that such a model does not naturally account for the SN Type Ic features seen in SN 2010gx and PTF09cnd at late times.

The shock breakout scenario predicts that the temperature will rise until luminosity maximum, and then decline after maximum (Ensman & Burrows 1992; CI11). Our temperature measurements (Figure 8) do not clearly follow this trend, appearing to be declining or flat before peak, although these early measurements are extremely noisy. Early detection and deep multi-band photometry will be required in the future to test this prediction of the shock breakout model in additional sources. It is also worth noting that the full hydrodynamic magnetar model carried out by KB10 makes a similar prediction for the temperature evolution (although our simplified model plotted in Figure 11 struggles to reproduce this feature), so early-time temperature measurements are unlikely to distinguish between the two models.

We also note that the definition of temperature becomes complex for the non-equilibrium conditions involved in shock breakout. Numerous works (e.g., Ensman & Burrows 1992; Katz et al. 2010; Nakar & Sari 2010) find that the radiation or color temperature of the shock breakout emission is higher than the effective temperature (defined by the luminosity surface density $L/4\pi r^2$). If this holds true in the case of SN 2005ap-like objects, it would increase the wind radius calculated here. The total mass expelled by the progenitor in a wind would increase, but other parameters like $D_{\star}$ and $E_{51}^2\ M_{\rm ej,10}$ would not be affected. Such a discrepancy may be necessary if the shock breakout model holds true, as the SN is predicted to expand for a time t_d *before* the light curve begins to rise (CI11). However, our measured radii for PS1-10awh and SCP 06F6 (Figure 8) are consistent with explosion at approximately Day −30, around the time the light curves begin to rise. A decrease in effective temperature by ∼40% (consistent with that predicted by Ensman & Burrows 1992) could increase the blackbody radii and provide space for expansion that begins at Day −60 rather that Day −30.

Also interesting within the shock breakout picture is the fact that the expansion velocities do not appear to decline over a 17 day baseline (Section 6). This might naturally be explained if, indeed, there is no CSM outside of the diffusion radius and therefore the swept-up shell is not undergoing substantial deceleration. However, this is perhaps an oversimplification, as we calculate r_w to be slightly larger than r_d. There is therefore the possibility of ongoing CSM interaction at later times, complicating our simple shock breakout picture from a truncated CSM. However, we must remember that these observations are sensitive to an uncertain temperature evolution and they are influenced by two independent light curves which have been spliced together.

7.3.1. Predicted Radio Emission

We can predict the radio signature for such a shock breakout from a dense wind using standard models of radio SNe (Chevalier 1996). While the shock front is inside r_d, it propagates as a radiation-dominated shock wave. This shock structure does not give rise to particle acceleration to relativistic energies, so no radio synchrotron emission will result in this early stage. If $r_w > r_d$ and the blast wave continues to interact with CSM after breakout, some particle acceleration might occur, but it would likely result in a relatively short-lived burst of radio emission, as r_w cannot be significantly larger than r_d if we are to explain the very high luminosities of SN 2005ap-like objects and the large drop from maximum observed in some objects (e.g., SN 2010gx). In addition, any radio emission will be heavily absorbed due to free–free processes (Weiler et al. 2002) and synchrotron self-absorption (Chevalier 1998), so any burst of radio emission will to be faint.

If the stellar wind is truncated as described above, the SN will then expand past the CSM. Even if relativistic particles and magnetic field had been present, their energy densities would rapidly decline due to adiabatic expansion, and the radio flux density would plummet as $S_{\nu} \propto t^{-6}$ (Shklovskii 1960). It is possible at this point that a viscous reverse shock develops, but the reverse shock is less powerful than the forward shock, the magnetic field is likely to be weak, and any accelerated particles are subject to loss processes (Coulomb, inverse Compton, and/or synchrotron), so that the reverse shock is unlikely to be a strong source of synchrotron emission. Therefore, after the shock expands past r_w, it is unlikely to be a source of radio emission; our EVLA non-detections are not surprising in light of this model.

Finally, we note that we do not expect bright radio emission from the magnetar spin-down scenario (Section 7.2). Even Galactic magnetars are typically not detected at radio wavelengths (e.g., Gaensler et al. 2001; Burgay et al. 2006), and the newborn magnetars proposed by KB10 will additionally suffer free–free absorption from the ionized ejecta in which they are embedded. We therefore do not expect SN 2005ap-like objects to be sources of radio emission, but only the future combination of deep optical time-domain searches with the Large Synoptic Survey Telescope (LSST; Ivezic et al. 2008) and accompanying blind radio transient surveys with the Australian Square Kilometre Array Pathfinder (Johnston et al. 2007) will fully test this hypothesis.

8. CONCLUSIONS

Using multi-color photometry and multi-epoch spectroscopy, we find that PS1-10ky and PS1-10awh radiate ∼10^{51} erg in just a few months, making them among the most energetic SNe known. Our estimates are consistent with the lower-redshift SN 2005ap-like sources presented in Q+11. The peak bolometric magnitude of PS1-10ky is −22.5 mag, as compared with −19.5 mag for Type Ia SNe (Contardo et al. 2000), −21.4 mag for the proposed pair-instability SN 2007bi (Gal-Yam et al. 2009; Young et al. 2010), and −21.8 mag for the ultraluminous Type IIn SN 2006gy (Ofek et al. 2007; Smith et al. 2007).

There is no evidence for decreasing radial velocity during the SN 2005ap-like phase in the objects studied here, consistent

with the expansion of an optically thick shell predicted by both the magnetar and circumstellar interaction scenarios. However, SN 2005ap itself provides a counter-example to this point, displaying a clear decrease in velocity (Quimby et al. 2007). A larger sample of objects with time series spectroscopy is required to test the prevalence of decelerating photospheric velocities in SN 2005ap-like objects. Two sources to date, SN 2010gx (Pastorello et al. 2010) and PTF09cnd (Q+11), have shown evidence for dissipation of the optically thick shell and decreases in optical depth, revealing SNe Ic in their interiors.

Here, we show that radioactive decay cannot explain PS1-10ky, consistent with the findings of Q+11 and ruling out pair-instability models (e.g., Barkat et al. 1967) for this particular class of ultraluminous SNe (unlike in the case of the unusually luminous SN 2007bi (Gal-Yam et al. 2009)). We investigate two physical scenarios that both require an energetic optically thick shell: the spin-down of a newborn magnetar or shock breakout from a dense CSM. Both scenarios can fit our data with plausible parameters for an SN Ic, although both require rather extreme additional conditions. If magnetars are responsible for SN 2005ap-like objects, they need to be spinning near breakup (1–2 ms period). Meanwhile, if shock breakout causes these events, the progenitor had likely undergone an LBV-like outburst, expelling several solar masses of H-poor material in just a few years before stellar death; however, no such violent eruption has ever been observed from the W-R stars that are likely the progenitors of these SNe (although dense He-rich CSM has been observed to be present around some Type Ib SNe; Pastorello et al. 2007; Foley et al. 2007).

One of the most promising strategies for distinguishing between these scenarios in the future is early-time measurement of the photospheric radius, because at the time of light curve rise in the CSM interaction model, the SN will expand from a relatively much larger radius as compared with the magnetar spin-down model. In addition, late-time spectroscopic observations have the potential to distinguish between the two models. For example, the later spectra of SN 2010gx and PTF09cnd may conflict with expectations from the magnetar model, as this scenario predicts that the SN ejecta themselves are being swept into a thin shell by the magnetar wind; however, relatively normal SN Ic ejecta are observed in these sources at late times. Finally, additional measurements of photospheric velocity can test the circumstellar interaction model, as this scenario makes simple predictions for the velocity related to measurable light curve parameters. In the cases of PS1-10ky and PS1-10awh, the simple circumstellar interaction model predicts velocities that are significantly lower than what we measure, but this could plausibly be a viewing angle effect if the CSM is distributed in a torus (or disk; Metzger 2010). Additional observations should reveal some SN 2005ap-like sources with significantly lower photospheric velocities, if this torus geometry is widespread.

Any model for SN 2005ap-like sources needs to explain why these ultraluminous events are only associated with a small fraction of SN explosions (<1 in 10,000 core-collapse SNe, according to Q+11); the extreme conditions implied by both models discussed here might justify their rarity, but it remains to be determined if we can expect such fast-spinning magnetars or dense H-poor circumstellar media in sufficient numbers to explain the rates of SN 2005ap-like sources. The lack of detection of host galaxies for PS1-10ky and PS1-10awh (down to $\sim$0.10 $L^{\star}$) implies that they are in dwarf galaxies with low metallicities and high specific SFRs. This is a common feature for these type of transients (Pastorello et al. 2010; Neill et al. 2011; Q+11). As none have been found in an $L^{\star}$-type galaxy, this may point to metallicity playing a key role in the progenitor channel—or it may simply be an artifact of the bulk of cosmic star formation occurring in systems with high specific SFR. A larger sample of SN 2005ap-like sources is required to distinguish between these scenarios. Moreover, we note that, given their limited brightnesses ($\sim$21 mag at peak at $z \approx 0.9$) and the widespread cutoff in luminosity blueward of 2500 Å, we believe SN 2005ap-like sources will be of limited utility for ultraviolet high-redshift absorption-line studies (e.g., Lyα), in contrast with the claims of Q+11.

While wide-field shallower surveys (e.g., PTF) will continue to discover SN 2005ap-like sources in the local Universe, PS1 has shown the complementary potential to reveal such events at higher redshift, currently discovering $\sim$1 such source each month at $z \gtrsim 0.5$. Detailed optical studies will continue to be carried out on local events, while SNe at $z \sim 1$ enable studies of the rest-frame UV properties—the hallmark of this peculiar class of explosions. Working together toward the era of LSST, we will test their diversity as a class and measure their rates as a function of redshift. Increased sample sizes at a range of redshifts will better constrain the physical properties of these highly energetic explosions, their host galaxies, and discern between the magnetar spin-down and shock breakout scenarios.

We thank S. Balberg, D. Kasen, B. Metzger, R. Quimby, and R. Stoll for helpful insights. Laura Chomiuk is a Jansky Fellow of the National Radio Astronomy Observatory. Ryan J. Foley is supported by a Clay Fellowship. This discovery was enabled using the PS1 System operated by the PS1 Science Consortium (PS1SC) and its member institutions. The PS1 Surveys have been made possible through the combinations of the Institute for Astronomy at the University of Hawaii, The Pan-STARRS Project Office, the Max-Planck Society and its participating institutes, the Max Planck Institute for Astronomy, Heidelberg, and the Max Planck Institute for Extraterrestial Physics, Garching, The Johns Hopkins University, the University of Durham, the University of Edinburgh, the Queen's University of Belfast, the Harvard-Smithsonian Center for Astrophysics, the Las Cumbres Observatory Global Network, and the National Central University of Taiwan. Observations reported here were obtained at the MMT Observatory, a joint facility of the Smithsonian Institution and the University of Arizona. This paper uses data products produced by the OIR Telescope Data Center, supported by the Smithsonian Astrophysical Observatory. The EVLA is run by the National Radio Astronomy Observatory, a facility of the National Science Foundation operated under cooperative agreement by Associated Universities, Inc.. Gemini Observatory is operated by the Association of Universities for Research in Astronomy, Inc., under a cooperative agreement with the NSF on behalf of the Gemini partnership: the National Science Foundation (United States), the Science and Technology Facilities Council (United Kingdom), the National Research Council (Canada), CONICYT (Chile), the Australian Research Council (Australia), Ministério da Ciência e Tecnologia (Brazil), and Ministerio de Ciencia, Tecnología e Innovación Productiva (Argentina). Some of the image processing in this paper was run on the Odyssey cluster supported by the FAS Science Division Research Computing Group at Harvard University. We appreciate the excellent support by the staffs at Gemini, MMT, EVLA, and PS1. We are grateful for access to Gemini under programs GN-2010A-Q-30 and GS-2010B-Q-4 (PI: E. Berger) and GN-2010B-Q-34 (PI: J. Tonry). Partial support for this work was

provided by National Science Foundation grants AST-1009749 and AST-0807727.

Facilities: PS1(GPC1), MMT (Blue Channel Spectrograph, Hectospec), Gemini:Gillett (GMOS), EVLA, GALEX

REFERENCES

Abazajian, K. N., Adelman-McCarthy, J. K., Ageros, M. A., et al. 2009, ApJS, 182, 543
Arnett, W. D. 1982, ApJ, 253, 785
Barbary, K., Dawson, K. S., Tokita, K., et al. 2009, ApJ, 690, 1358
Barkat, Z., Rakavy, G., & Sack, N. 1967, Phys. Rev. Lett., 18, 379
Berger, E., Kulkarni, S. R., Pooley, G., et al. 2003, Nature, 426, 154
Burgay, M., Rea, N., Israel, G. L., et al. 2006, MNRAS, 372, 410
Cardelli, J. A., Clayton, G. C., & Mathis, J. S. 1989, ApJ, 345, 245
Chatzopoulos, E., Wheeler, J. C., & Vinko, J. 2009, ApJ, 704, 1251
Chevalier, R. A. 1996, in ASP Conf. Ser. 93, Radio Emission from the Stars and the Sun, ed. A. R. Taylor & J. M. Paredes (San Francisco, CA: ASP), 125
Chevalier, R. A. 1998, ApJ, 499, 810
Chevalier, R. A., & Irwin, C. M. 2011, ApJ, 729, L6
Christensen, L., Hjorth, J., & Gorosabel, J. 2004, A&A, 425, 913
Contardo, G., Leibundgut, B., & Vacca, W. D. 2000, A&A, 359, 876
Davidson, K., & Humphreys, R. M. 1997, ARA&A, 35, 1
Drout, M. R., Soderberg, A. M., Gal-Yam, A., et al. 2010, arXiv:1011.4959
Ensman, L., & Burrows, A. 1992, ApJ, 393, 742
Faber, S. M., Willmer, C. N. A., Wolf, C., et al. 2007, ApJ, 665, 265
Fabricant, D., Fata, R., Roll, J., et al. 2005, PASP, 117, 1411
Foley, R. J., Smith, N., Ganeshalingam, M., et al. 2007, ApJ, 657, L105
Frail, D. A., Kulkarni, S. R., Berger, E., & Wieringa, M. H. 2003, AJ, 125, 2299
Frail, D. A., Soderberg, A. M., Kulkarni, S. R., et al. 2005, ApJ, 619, 994
Fruchter, A. S., Levan, A. J., Strolger, L., et al. 2006, Nature, 441, 463
Gaensler, B. M., Slane, P. O., Gotthelf, E. V., & Vasisht, G. 2001, ApJ, 559, 963
Gal-Yam, A., Mazzali, P., Ofek, E. O., et al. 2009, Nature, 462, 624
Gänsicke, B. T., Levan, A. J., Marsh, T. R., & Wheatley, P. J. 2009, ApJ, 697, L129
Gezari, S., Halpern, J. P., Grupe, D., et al. 2009, ApJ, 690, 1313
Hodapp, K. W., Siegmund, W. A., Kaiser, N., et al. 2004, Proc. SPIE, 5489, 667
Hogg, D. W., Baldry, I. K., Blanton, M. R., & Eisenstein, D. J. 2002, arXiv:0210394
Hook, I. M., Jørgensen, I., Allington-Smith, J. R., et al. 2004, PASP, 116, 425
Immler, S., Modjaz, M., Landsman, W., et al. 2008, ApJ, 674, L85
Ivezic, Z., Tyson, J. A., Acosta, E., et al. 2008, arXiv:0805.2366
Jeffery, D. J., & Branch, D. 1990, in Supernovae, Jerusalem Winter School for Theoretical Physics, ed. J. C. Wheeler, T. Piran, & S. Weinberg (Singapore: World Scientific), 149
Johnston, S., Bailes, M., Bartel, N., et al. 2007, PASA, 24, 174
Kaiser, N., Burgett, W., Chambers, K., et al. 2010, Proc. SPIE, 7733, 77330E-1
Kasen, D., & Bildsten, L. 2010, ApJ, 717, 245
Katz, B., Budnik, R., & Waxman, E. 2010, ApJ, 716, 781
Kennicutt, R. C., Jr. 1998, ARA&A, 36, 189
Kewley, L. J., Geller, M. J., & Jansen, R. A. 2004, AJ, 127, 2002
Kocevski, D., & West, A. A. 2011, ApJ, 735, L8
Kulkarni, S. R., Frail, D. A., Wieringa, M. H., et al. 1998, Nature, 395, 663
Le Floc'h, E., Duc, P.-A., Mirabel, I. F., et al. 2003, A&A, 400, 499
MacFadyen, A. I., & Woosley, S. E. 1999, ApJ, 524, 262
Magnier, E. 2006, in Proceedings of The Advanced Maui Optical and Space Surveillance Technologies Conference, ed. S. Ryan (Kihei, HI: The Maui Economic Development Board), E50
Malesani, D., Fynbo, J. P. U., Hjorth, J., et al. 2009, ApJ, 692, L84
Mannucci, F., Salvaterra, R., & Campisi, M. A. 2011, MNRAS, 414, 1263
Metzger, B. D. 2010, MNRAS, 409, 284
Miller, A. A., Chornock, R., Perley, D. A., et al. 2009, ApJ, 690, 1303
Mink, D. J., Wyatt, W. F., Caldwell, N., et al. 2007, in ASP Conf. Ser. 376, Astronomical Data Analysis Software and Systems XVI, ed. R. A. Shaw, F. Hill, & D. J. Bell (San Francisco, CA: ASP), 249
Modjaz, M., Li, W., Butler, N., et al. 2009, ApJ, 702, 226
Nakar, E., & Sari, R. 2010, ApJ, 725, 904
Neill, J. D., Sullivan, M., Gal-Yam, A., et al. 2011, ApJ, 727, 15
Nugis, T., & Lamers, H. J. G. L. M. 2000, A&A, 360, 227
Ofek, E. O., Cameron, P. B., Kasliwal, M. M., et al. 2007, ApJ, 659, L13
Onaka, P., Tonry, J. L., Isani, S., et al. 2008, Proc. SPIE, 7014, 70140D-1
Pastorello, A., Smartt, S. J., Botticella, M. T., et al. 2010, ApJ, 724, L16
Pastorello, A., Smartt, S. J., Mattila, S., et al. 2007, Nature, 447, 829
Perley, R. A., Chandler, C. J., Butler, B. J., & Wrobel, J. M. 2011, ApJ, 739, L1
Phillips, M. M. 1993, ApJ, 413, L105
Quimby, R. M., Aldering, G., Wheeler, J. C., et al. 2007, ApJ, 668, L99
Quimby, R. M., Kulkarni, S. R., Kasliwal, M. M., et al. 2011, Nature, 474, 487
Rest, A., Stubbs, C., Becker, A. C., et al. 2005, ApJ, 634, 1103
Schlegel, D. J., Finkbeiner, D. P., & Davis, M. 1998, ApJ, 500, 525
Schmidt, G. D., Weymann, R. J., & Foltz, C. B. 1989, PASP, 101, 713
Shklovskii, I. S. 1960, SvA, 4, 243
Smith, N., Li, W., Foley, R. J., et al. 2007, ApJ, 666, 1116
Smith, N., & McCray, R. 2007, ApJ, 671, L17
Smith, N., & Owocki, S. P. 2006, ApJ, 645, L45
Soker, N., Frankowski, A., & Kashi, A. 2010, New Astron., 15, 189
Stoll, R., Prieto, J. L., Stanek, K. Z., et al. 2011, ApJ, 730, 34
Stubbs, C. W., Doherty, P., Cramer, C., et al. 2010, ApJS, 191, 376
Tonry, J., & Onaka, P. 2009, in Advanced Maui Optical and Space Surveillance Technologies Conference, ed. S. Ryan (Kihei, HI: The Maui Economic Development Board), E40
Tremonti, C. A., Heckman, T. M., Kauffmann, G., et al. 2004, ApJ, 613, 898
Valenti, S., Benetti, S., Cappellaro, E., et al. 2008, MNRAS, 383, 1485
van der Horst, A. J., Rol, E., Wijers, R. A. M. J., et al. 2005, ApJ, 634, 1166
Weiler, K. W., Panagia, N., Montes, M. J., & Sramek, R. A. 2002, ARA&A, 40, 387
Woosley, S. E. 2010, ApJ, 719, L204
Woosley, S. E., Blinnikov, S., & Heger, A. 2007, Nature, 450, 390
York, D. G., Adelman, J., Anderson, J. E., Jr., et al. 2000, AJ, 120, 1579
Young, D. R., Smartt, S. J., Valenti, S., et al. 2010, A&A, 512, A70